

**INTEGRATION OF GEOMETRY AND SMALL AND LARGE DEFORMATION
ANALYSIS FOR VEHICLE MODELLING: CHASSIS, AND AIRLESS AND
PNEUMATIC TIRE FLEXIBILITY**

Mohil D. Patel¹ (mpate72@uic.edu)
Carmine M. Pappalardo² (cpappalardo@unisa.it)
Gengxiang Wang³ (gengxiangwang@gmail.com)
Ahmed A. Shabana¹ (shabana@uic.edu)

¹ Department of Mechanical and Industrial Engineering, University of Illinois at Chicago,
Chicago, IL 60607, USA

² Department of Industrial Engineering, University of Salerno, Fisciano (Salerno), 84084, Italy

³ Faculty of Mechanical and Precision Instrument Engineering, Xi'an University of Technology,
Xi'an 710048, Shaanxi, P.R. China

ABSTRACT

The goal of this study is to propose an approach for developing new and detailed vehicle models that include flexible components with complex geometries, including chassis, and airless and pneumatic tires with distributed inertia and flexibility. The methodology used is based on successful integration of geometry, and small and large deformation analysis using a mechanics-based approach. The *floating frame of reference* (FFR) formulation is used to model the small deformations, whereas the *absolute nodal coordinate formulation* (ANCF) is used for the large deformation analysis. Both formulations are designed to correctly capture complex geometries including structural discontinuities. To this end, a new ANCF-preprocessing approach based on linear constraints that allows for systematically eliminating dependent variables and significantly reducing the component model dimension is proposed. One of the main contributions of this paper is the development of the first ANCF airless tire model which is integrated in a three-dimensional multibody system (MBS) algorithm designed for solving the differential/algebraic equations of detailed vehicle models. On the other hand, relatively stiff components with complex geometries, such as the vehicle chassis, are modeled using the finite element (FE) FFR formulation which creates a local linear problem that can be exploited to eliminate high frequency and insignificant deformation modes. Numerical examples that include a simple ANCF pendulum with structural discontinuities and a detailed off-road vehicle model consisting of flexible tires and chassis are presented. Three different tire types are considered in this study; a brush-type tire, a pneumatic FE/ANCF tire, and an airless FE/ANCF tire. The numerical results are obtained using the general purpose MBS computer program **SIGMA/SAMS** (Systematic Integration of Geometric Modeling and Analysis for the Simulation of Articulated Mechanical Systems).

Keywords: Airless tires; pneumatic tires; absolute nodal coordinate formulation; floating frame of reference formulation; integration of computer-aided design and analysis (I-CAD-A).

1. INTRODUCTION

This investigation is concerned with the development of new detailed MBS small- and large-deformation vehicle models consisting of components with complex geometries including structural discontinuities. In this section, research background, brief literature review, the scope, contributions, and organization of the paper are discussed.

1.1 Background

Despite the fact that computational rigid MBS algorithms have been widely used in the analysis of vehicle systems since the 1980s [1, 2], incorporating component flexibility is necessary in order to develop high fidelity vehicle models that can be effectively used in accurate and reliable durability investigations. The FE/FFR formulation, introduced in the early 1980's for the small-deformation analysis of MBS applications with structural discontinuities [3], leads to accurate representation of the nonlinear inertia forces and coupling between the reference and elastic displacements. An example of a vehicle component with structural discontinuities is the chassis depicted in Fig. 1 which shows slope discontinuities at several locations in which beam structures are connected. Because in FFR formulation, the FE deformation is described in the body coordinate system and the large rotation and translation of the flexible body are described using the local body coordinate system which serves as the body reference, the FE/FFR formulation allows using non-isoparametric elements with large-rotation non-incremental MBS solution procedures.

The analysis of the large deformation, on the other hand, can be accomplished using the *absolute nodal coordinate formulation* (ANCF) [4 – 6]. ANCF elements employ gradient vectors instead of infinitesimal rotations as nodal coordinates, allowing for exact description of rigid body motion even in the case of beam, plate, and shell elements. ANCF elements have several desirable

features that include constant mass matrix and zero Coriolis and centrifugal inertia force vectors, which are highly nonlinear in the FFR formulation. Fully parameterized ANCF elements, in particular, can be used to systematically describe structural discontinuities of components made of relatively softer materials such as tires. Figure 2 depicts two different types of tires that will be considered in this investigation. The first is a pneumatic tire which has smooth nominal geometry, while the second is an airless tire which has slope discontinuities. The fact that there is no distinction between plate and shell structures when ANCF elements are used allows for developing complex geometry models by proper selection of the nodal coordinates in the reference configuration.

MBS dynamics, widely used in the analysis of wheeled vehicles [7], provides significant insight on the design and performance of the vehicle before a working prototype can be manufactured. While the FE/FFR formulation was introduced more than three decades ago, long before ANCF elements were introduced, there exists a large number of vehicle applications in which the use of the small-deformation FE/FFR formulation can contribute to developing accurate and efficient computer models, particularly when combined with an ANCF large-deformation approach. Efficient modeling of vehicle systems that include stiff chassis and more flexible tires will require efficient implementation of both methods in computational MBS algorithms. The two methods, however, employ two fundamentally different approaches for the treatment of structural discontinuities. In the FE/FFR approach, in which infinitesimal rotations are used as nodal coordinates, a conventional vector coordinate transformation is used; while in the ANCF approach, in which gradients are used as nodal coordinates, a gradient transformation must be used to account for the effect of structural discontinuities. In the FFR approach, an intermediate element coordinate system must be introduced, while the ANCF approach does not require the use of such an

intermediate coordinate system for the treatment of structural discontinuities because of the use of the position vector gradients.

1.2 Literature Review

Several vehicle components like the chassis shown in Fig. 1 are typically modeled using the FE/FFR approach since a small-deformation assumption can be made. The FE/FFR formulation was used to study the nonlinear dynamics of a vehicle traversing over an obstacle with the goal of examining the chassis deformation [8]. The FFR three-dimensional beam element was used to model the chassis of a dune buggy subjected to external excitation through a half-sine function based road bump [9]. Ambrosio and Goncalves [10] compared the results of the rigid and flexible chassis models of a detailed sport vehicle undergoing various maneuver tests. Sampo [11] studied the dynamics of a formula student vehicle by considering the chassis flexibility. Shiiba et al. [12] investigated the effect of using several non-modal model-order reduction techniques on the flexible chassis of a detailed racing vehicle model with specific emphasis on ride characteristics. Carpinelli et al. [13] compared rigid and flexible body models for the prediction of ride and handling characteristics of a commercial sedan vehicle. Goncalves and Ambrosio [14] optimized the suspension spring and damper coefficients of a wheeled vehicle that included a flexible chassis.

Another deformable vehicle component whose behavior has significant effect on the vehicle performance is the tire whose behavior is characterized by large rotation and deformation. Several tire models have been proposed over the past two decades for use with MBS vehicle models. These include formula-based curve-fitted, discrete mass-spring-damper-based, and FE-based models [15 – 17]. The formula-based tire models are typically used for vehicle dynamics simulations where the analysis is concerned with low-frequency tire and vehicle dynamics. The *Magic Formula* tire model proposed by Pacejka [15] is an example of a widely used formula-based tire model. The

discrete mass-spring-damper models yield better fidelity and are typically used in ride quality and durability simulations. Several commercial MBS software have implemented the discrete mass-spring-damper-based FTire model proposed by Gisper [16]. The FE-based tire models can capture a larger spectrum of frequency response and are also used for NVH (noise-vibration-harshness) and durability analyses where the tire high frequency response and stress is studied as well [17]. While there is a very large number of investigations on the FE modeling of tires, there is a relatively small number of investigations that couple FE tires and MBS vehicle models without the use of co-simulation techniques. A new ANCF method of tire-rim assembly was recently proposed [18], and was used by Patel et al. [4] to develop a new tire model in which the tire was modeled using ANCF plate/shell elements and the rim was modeled using the ANCF reference node. Recuero et al. [5] demonstrated the use of ANCF elements in the simulation of the tire/soil interaction, whereas Pappalardo et al. used the rational ANCF elements [19] and the so-called consistent rotation-based formulation (ANCF/CRBF) elements [20] to model the tire. Yamashita et al. [21] modeled the tire using the bilinear ANCF shell element and demonstrated braking and cornering scenarios with the tire model. Sugiyama and Suda [22] modeled the tire as a ring-type structure using planar curved ANCF beam elements and compared its vibration modes with analytical and experimental results. Recuero et al. [23] examined the tire-soil interaction using a co-simulated rigid body vehicle model, FE tire model that utilized bilinear shell elements, and DEM (discrete element method) soil model.

1.3 Scope, Contributions, and Organization of the Paper

This paper focuses on developing a computational framework based on the integration of geometry and small- and large-deformation analysis for the nonlinear dynamics of detailed vehicle models that consist of rigid and flexible bodies. The proposed approach captures accurately structural

discontinuities that characterize the chassis (as the one shown in Fig. 1) and airless tires (shown in Fig. 2). In this geometry-based approach, the chassis and tires are modeled as flexible bodies using the small-deformation FFR and large-deformation ANCF elements, respectively. Specifically, the main contributions of the paper can be summarized as follows:

1. The first ANCF airless tire model with distributed inertia and elasticity is developed in this investigation and integrated with computational MBS algorithms without the need for using *co-simulation techniques*. The FE model accurately captures the structural discontinuities that characterize this tire type.
2. An approach for vehicle assembly based on the integration of rigid body, small-deformation FFR, and large-deformation ANCF algorithms is proposed for developing new and detailed vehicle models. Stiff components such as the chassis are modeled using FFR elements, while more flexible components such as the tires are modeled using ANCF elements.
3. A new method for the treatment of structural discontinuities using ANCF elements is proposed. In the new approach, linear algebraic constraint equations are formulated at a preprocessing stage, thereby allowing for systematically reducing the model dimension by eliminating dependent variables before the start of the dynamic simulation.
4. The paper introduces a damping model for ANCF pneumatic tires which accounts for the energy dissipation in the tire material as well as due to the pressurized air in a tire model.
5. New **high-mobility multi-purpose wheeled vehicle (HMMWV)** models are developed in this investigation. In one model, airless tires are used, while in a second model pneumatic tires are used. Both tires models are described using ANCF elements. In the vehicle models developed, the chassis is modeled using FFR elements, and a component-mode synthesis method is used to eliminate insignificant high frequency modes.

6. Using the HMMWV model, the paper presents a comparative study based on three different vehicle models. The first model is the vehicle with brush-type tires, the second is a vehicle with pneumatic tires, and the third is a vehicle with airless tires. The results obtained using these three different models are compared.

The sections of the paper are organized as follows. Section 2 briefly describes the two finite element formulations used to model the small- and large-deformations of the flexible components used in the vehicle system. The FE/FFR method will be used to model small-deformation behavior, whereas ANCF elements will be used to model the large deformation behavior. Section 3 describes the FFR and ANCF methods used to account for structural discontinuities. Section 4 discusses the MBS equations of motion of the vehicle system. Section 5 presents two numerical examples; the first example demonstrates the use of the linear ANCF constraint equations in modeling structural discontinuities and the second example is the HMMWV vehicle model with an FE/FFR chassis and ANCF tires. Three types of tire models, brush-type rigid tire, pneumatic ANCF tire, and an airless ANCF tire, are used and the results obtained are compared.

2. SMALL- AND LARGE-DEFORMATION ANALYSIS

Accurate and efficient modeling of vehicle system applications requires the integration of small- and large-deformation formulations. The stresses of relatively stiff components such as rods and chassis can be efficiently modeled using a small-deformation formulation that allows for systematically eliminating insignificant deformation modes. More flexible components such as tires and belt drives, on the other hand, require the use of a large-deformation formulation. This section briefly discusses the two formulations used to describe the component flexibility in this paper. These two fundamentally different formulations, FFR and ANCF, are integrated in one

MBS computational algorithm designed for solving the differential/algebraic equations that govern the dynamics of vehicle systems. The brief presentation in this and the following sections is necessary in order to have an understanding of the fundamental differences between the two formulations in the way the coordinates are selected and the structural discontinuities are handled. In the FE/FFR method, a conventional coordinate transformation based on orthogonal transformation matrices is used; while for ANCF elements, transformation between parameters or coordinate lines is used leading to a non-orthogonal gradient transformation.

2.1 FE/FFR Formulation

In the FFR formulation, the absolute position vector of an arbitrary point on body i can be written as $\mathbf{r}^i = \mathbf{R}^i + \mathbf{A}^i \bar{\mathbf{u}}^i$, where \mathbf{R}^i is the absolute position vector of body reference, \mathbf{A}^i is the rotation matrix that defines the orientation of the body reference, and $\bar{\mathbf{u}}^i$ is the local position vector of the arbitrary point. If the body is deformable, the absolute position vector can be written as $\mathbf{r}^i = \mathbf{R}^i + \mathbf{A}^i (\bar{\mathbf{u}}_0^i + \bar{\mathbf{u}}_f^i)$, where $\bar{\mathbf{u}}_0^i$ is the local position vector of the point in the undeformed state and $\bar{\mathbf{u}}_f^i$ is the time-dependent deformation vector.

Beam elements will be used in this study to model the chassis in the FE/FFR formulation. The displacement field of the beam element can be written as $\mathbf{w} = \mathbf{S}\mathbf{e}$, where \mathbf{S} is the element shape function matrix and \mathbf{e} is the vector of the element nodal coordinates. The shape function matrix of the FE/FFR beam element is provided in Appendix A.1. In order to be able to correctly model structural discontinuities in the FE/FFR formulation, four coordinate systems are used: the global coordinate system (GCS), body coordinate system (BCS), intermediate coordinate system (ICS), and the element coordinate system (ECS) as shown in Fig. 3. For every ECS, there exists an ICS which is initially parallel to the ECS and fixed with respect to the BCS. Using the concept of the ICS, the beam displacement field of an element j on body i can be written in the ICS as

$\mathbf{w}_{ICS}^{ij} = \mathbf{S}^{ij} \mathbf{e}_{ICS}^{ij}$, where the subscript ICS refers to vectors defined in ICS. Furthermore, \mathbf{e}_{ICS}^{ij} can be written in terms of the nodal coordinates described in BCS as $\mathbf{e}_{ICS}^{ij} = \bar{\mathbf{C}}^{ij} \mathbf{q}_n^{ij}$, where \mathbf{q}_n^{ij} is the vector of nodal coordinates described in BCS, and $\bar{\mathbf{C}}^{ij}$ is a constant transformation matrix between ICS and BCS, composed of orthogonal transformation matrices. The location of the point in the BCS can be written as $\bar{\mathbf{u}}^{ij} = \mathbf{C}^{ij} \mathbf{w}_{ICS}^{ij}$ or $\bar{\mathbf{u}}^{ij} = \mathbf{C}^{ij} \mathbf{S}^{ij} \bar{\mathbf{C}}^{ij} \mathbf{q}_n^{ij}$, where \mathbf{C}^{ij} is an orthogonal transformation matrix that defines the ICS with respect to the BCS. The nodal coordinates of element j can be written in terms of the total vector of nodal coordinates of the body as $\mathbf{q}_n^{ij} = \mathbf{B}_1^{ij} \mathbf{q}_n^i$, where \mathbf{B}_1^{ij} is a Boolean matrix that defines the connectivity between finite elements forming the flexible body. Consequently, the local position vector can be written as $\bar{\mathbf{u}}^{ij} = \mathbf{C}^{ij} \mathbf{S}^{ij} \bar{\mathbf{C}}^{ij} \mathbf{B}_1^{ij} \mathbf{q}_n^i$ [3, Chapter 6]. In order to define a unique displacement field by eliminating the rigid body modes of the element shape function matrix, a set of *reference conditions* must be applied. To this end, the body nodal coordinates are written as $\mathbf{q}_n^i = \mathbf{q}_0^i + \bar{\mathbf{q}}_f^i$, where \mathbf{q}_0^i is the vector of body nodal coordinates in the un-deformed configuration and $\bar{\mathbf{q}}_f^i$ is the vector of body nodal deformations which can be written as $\bar{\mathbf{q}}_f^i = \mathbf{B}_2^i \mathbf{q}_f^i$, where \mathbf{B}_2^i is the linear transformation matrix obtained using the reference conditions. Using the transformation $\bar{\mathbf{q}}_f^i = \mathbf{B}_2^i \mathbf{q}_f^i$, the local position vector $\bar{\mathbf{u}}^{ij}$ can be written as $\bar{\mathbf{u}}^{ij} = \mathbf{C}^{ij} \mathbf{S}^{ij} \bar{\mathbf{C}}^{ij} \mathbf{B}_1^{ij} (\mathbf{q}_0^i + \mathbf{B}_2^i \mathbf{q}_f^i) = \mathbf{N}^{ij} (\mathbf{q}_0^i + \mathbf{B}_2^i \mathbf{q}_f^i) = \mathbf{N}^{ij} \mathbf{q}_n^i$.

The analysis presented in this section shows that assembly of elements that have different orientations in the reference configuration requires the use of constant orthogonal transformation matrices (\mathbf{C}^{ij} and $\bar{\mathbf{C}}^{ij}$). The use of these transformations in the FE/FFR formulation is necessary in order to have exact modeling of the rigid body dynamics. In the FE/FFR formulation, the vector of body generalized coordinates is written as $\mathbf{q}^i = [\mathbf{R}^{iT} \quad \boldsymbol{\theta}^{iT} \quad \mathbf{q}_f^{iT}]^T$, where \mathbf{R}^i and $\boldsymbol{\theta}^i$ are the

body reference translation and rotational coordinates, respectively. The kinetic energy can be defined using the generalized velocities and the body mass matrix as

$$T^i = \frac{1}{2} \dot{\mathbf{q}}^{iT} \mathbf{M}^i \dot{\mathbf{q}}^i = \frac{1}{2} \dot{\mathbf{q}}^{iT} \left[\sum_{j=1}^{n_e} \mathbf{M}^{ij} \right] \dot{\mathbf{q}}^i, \text{ where } n_e \text{ is the number of elements, } \mathbf{M}^{ij} \text{ is the mass matrix}$$

of element j , and \mathbf{M}^i is the body mass matrix which is a highly nonlinear function of the

coordinates. The virtual work of the elastic forces is defined as $\delta W_s^{ij} = - \int_{V^{ij}} \delta \boldsymbol{\epsilon}^{ijT} \boldsymbol{\sigma}^{ij} dV^{ij}$, where a

linear elastic and isotropic material is assumed for the stress-strain relationship. The element

stiffness matrix can be written as $\mathbf{K}_{ff}^{ij} = \int_{V^{ij}} \mathbf{V}^{ijT} \mathbf{E}^{ij} \mathbf{V}^{ij} dV^{ij}$, where $\mathbf{V}^{ij} = \mathbf{D}^{ij} \mathbf{N}^{ij} \mathbf{B}_2^i$, \mathbf{E}^{ij} is the matrix

of elastic coefficients, and \mathbf{D}^{ij} is the differential operator that relates the strains and displacements,

such that $\boldsymbol{\epsilon}^{ij} = \mathbf{D}^{ij} \bar{\mathbf{u}}_f^{ij}$. Using the transformations previously developed in this section, the element

stiffness matrices can be assembled to obtain the stiffness matrix \mathbf{K}_{ff}^i which can be used to define

the stiffness matrix \mathbf{K}^i associated with the total vector of coordinates of the body [3]. Using the

mass and stiffness matrices, the FE/FFR equations of motion for an unconstrained body i can be

written as

$$\mathbf{M}^i \ddot{\mathbf{q}}^i + \mathbf{K}^i \mathbf{q}^i = \mathbf{Q}_e^i + \mathbf{Q}_v^i \quad (1)$$

where \mathbf{Q}_e^i is the vector of generalized external forces, and \mathbf{Q}_v^i is the Coriolis and centrifugal

quadratic velocity vector. For flexible vehicle components with complex geometry such as the

chassis shown in Fig. 1, the number of elastic coordinates in Eq. 1 can be very large. For this

reason, coordinate reduction techniques are often used to reduce the problem dimensionality. In

this investigation, the number of elastic coordinates of the chassis is reduced using component

mode synthesis methods by performing an eigenvalue analysis of the system $\mathbf{M}_{ff}^i \ddot{\mathbf{q}}_f^i + \mathbf{K}_{ff}^i \mathbf{q}_f^i = \mathbf{0}$,

where \mathbf{M}_{ff}^i is the partition of the mass matrix associated with the vector of body nodal

deformations. Because of the application of the reference conditions, the stiffness matrix \mathbf{K}_{ff}^i is a symmetric positive-definite matrix [3]. Using the eigenvalue analysis, the vector of nodal coordinates can be written as $\mathbf{q}_f^i = \bar{\mathbf{B}}_m^i \mathbf{p}_f^i$, where $\bar{\mathbf{B}}_m^i$ is the modal transformation matrix whose columns contain the eigenvectors that represent significant deformation modes, and \mathbf{p}_f^i is the vector of modal coordinates. Because insignificant high frequency mode shapes are eliminated from $\bar{\mathbf{B}}_m^i$, the number of elastic coordinates can be significantly reduced as demonstrated by the HMMWV example used in this investigation.

2.2 ANCF Finite Elements

Unlike the FE/FFR formulation, ANCF elements lead to highly nonlinear elastic forces and a constant mass matrix, and therefore, the Coriolis and centrifugal inertia forces are zero when these elements are used. ANCF coordinates consist of position and gradient/slope vectors that are defined in the global coordinate system. Several ANCF elements have been proposed in the literature. These ANCF elements include beam, plate/shell, solid, triangular, and tetrahedral elements that can be defined using non-rational or rational polynomials [24 -28, 6]. When ANCF elements are used, the global position vector of an arbitrary point on element j of body i can be written using the element shape functions and nodal coordinates as $\mathbf{r}^{ij} = \mathbf{S}^{ij} \mathbf{e}^{ij}$, where \mathbf{S}^{ij} is the element shape function matrix, and \mathbf{e}^{ij} is the vector of element nodal coordinates. In this investigation, both pneumatic and airless tires will be modeled using ANCF plate/shell elements whose shape functions are provided in Appendix A.2. The vector of the four-node plate/shell element nodal coordinates \mathbf{e}^{ij} can be written as $\mathbf{e}^{ij} = [\mathbf{e}_1^{ijT} \quad \mathbf{e}_2^{ijT} \quad \mathbf{e}_3^{ijT} \quad \mathbf{e}_4^{ijT}]^T$, where the coordinates of node n can be written in the case of a fully-parameterized element as

$$\mathbf{e}_n^{ij} = \begin{bmatrix} \mathbf{r}_n^{ijT} & (\partial \mathbf{r}_n^{ij} / \partial x)^T & (\partial \mathbf{r}_n^{ij} / \partial y)^T & (\partial \mathbf{r}_n^{ij} / \partial z)^T \end{bmatrix}^T, \quad n = 1, 2, 3, 4, \quad \text{where} \quad \mathbf{x} = [x \quad y \quad z]^T \quad \text{are}$$

element parameters. No distinction is made between ANCF plate and shell elements because an ANCF shell element has the same assumed displacement field of the ANCF plate element. The shell geometry can be systematically defined using the element nodal coordinates in the reference configuration \mathbf{e}_0^{ij} , where the subscript 0 refers to reference configuration. The use of the position vector gradients as nodal coordinates allows for obtaining complex shell geometry by a proper choice of \mathbf{e}_0^{ij} . The mass matrix of ANCF elements $\mathbf{M}^{ij} = \int_{V_0^{ij}} \rho^{ij} \mathbf{S}^{ijT} \mathbf{S}^{ij} dV_0^{ij}$ can be defined using the kinetic energy, where ρ^{ij} and V_0^{ij} are, respectively, the mass density and volume in the reference configuration. Given an external force vector \mathbf{f}_e^{ij} , the ANCF generalized force vector can be written as $\mathbf{Q}_e^{ij} = \mathbf{S}^{ijT} \mathbf{f}_e^{ij}$. For fully parameterized ANCF elements, the continuum mechanics approach can be used to formulate the elastic forces. Given an elastic energy potential function U^{ij} , the second Piola-Kirchhoff stress tensor can be written as $\boldsymbol{\sigma}_{p2}^{ij} = \partial U^{ij} / \partial \boldsymbol{\epsilon}^{ij}$, where $\boldsymbol{\epsilon}^{ij} = (\mathbf{J}^{ijT} \mathbf{J}^{ij} - \mathbf{I}) / 2$ is the Green-Lagrange strain tensor, $\mathbf{J}^{ij} = \partial \mathbf{r}^{ij} / \partial \mathbf{X}^{ij}$ is the matrix of position vector gradients, and $\mathbf{X}^{ij} = \mathbf{S}^{ij} \mathbf{e}_0^{ij}$ is the vector of the element parameters in the reference configuration. The vector of element elastic forces can be formulated based on a hyper-elastic model as $\mathbf{Q}_k^{ij} = - \int_{V_0^{ij}} \left(\partial \boldsymbol{\epsilon}_v^{ij} / \partial \mathbf{e}^{ij} \right)^T \boldsymbol{\sigma}_v^{ij} dV_0^{ij}$, where the subscript v refers to Voigt (engineering) notation of the strain and stress tensors. In case of ANCF, the equations of motion of an unconstrained ANCF body i can be written as $\mathbf{M}^{i::i} \ddot{\mathbf{e}}^i = \mathbf{Q}_k^i + \mathbf{Q}_e^i$, where \mathbf{Q}_e^i is the vector of external forces.

As previously mentioned, ANCF plate/shell elements are used in this investigation to obtain accurate initially-curved geometry description for both pneumatic and airless tires. The stress-free initially-curved geometry in the reference configuration can be achieved by writing the matrix of position vector gradients as $\mathbf{J} = \mathbf{J}_e \mathbf{J}_0^{-1}$, where $\mathbf{J}_e = \partial \mathbf{r} / \partial \mathbf{x}$, $\mathbf{J}_0 = \partial \mathbf{X} / \partial \mathbf{x}$, $\mathbf{x} = [x \ y \ z]^T$ is vector of element coordinates in the straight configuration, and $\mathbf{X} = \mathbf{S} \mathbf{e}_0$ as previously defined. With the appropriate selection of \mathbf{e}_0 , curved structures can be easily modeled using ANCF elements. Additionally, volume transformation can be written between the straight and initially-curved configuration as $dV_0 = |\mathbf{J}_0| dV$ [29, 30, 6], where V and V_0 is the volume in the straight and reference configurations, respectively.

3. FFR AND ANCF MODELING OF STRUCTURAL DISCONTINUITIES

Structural discontinuities appear at the locations of intersection of rigidly-connected segments which have different orientations. These discontinuities characterize vehicle system components such as the chassis shown in Fig. 1 and the airless tire shown in Fig. 2. In order to develop accurate computational models for these components in MBS applications, it is necessary to use approaches that account for the slope discontinuities. This section briefly describes the methods used for handling structural discontinuities in the two FE formulations used in this investigation. A new ANCF approach for the treatment of structural discontinuities is also proposed in this section. In this approach, a constant velocity transformation matrix is developed and used to eliminate the dependent variables at a preprocessing stage. The new approach offers the flexibility and generality of combining structural discontinuity constraints with other constraints since it retains the original element coordinates before any coordinate transformation is performed.

3.1 FE/FFR Formulation

The element intermediate coordinate system (ICS) used in the FE/FFR formulation plays a crucial role in modeling structural discontinuities. The ICS concept is similar to that of the parallel axis theorem used in rigid body dynamics [3]. Consider the structure shown in Fig. 4 that consists of two non-isoparametric beam elements forming an L-shaped structural discontinuity at their intersection. For brevity, BCS, ECS and ICS in Fig. 4 refer to body, element, and intermediate coordinate systems, respectively. It can be seen from Fig. 4 that the orientation of ECS-1 (corresponding to element 1) is the same as that of the BCS, while the orientation of ECS-2 (corresponding to element 2) is different from that of the BCS. The shape functions of the non-isoparametric beam element used can correctly capture rigid body translation but, since this element uses infinitesimal rotations as nodal degrees of freedom, large finite rotations cannot be correctly modeled. In order to correctly capture the inertia of this structure and obtain correct rigid body kinematics, two ICSs are introduced at the BCS which are parallel to their respective ECS as shown in Fig. 4. The nodal coordinates defined in the BCS corresponding to each of the two elements can be transformed into their respective ICSs using the $\bar{\mathbf{C}}^{ij}$ matrix used in Section 2.1. Using this transformation, the shape function matrix of the non-isoparametric beam element can be used to yield the correct position of the material points with respect to the ICS. The position of the material point obtained in the ICS can then be transformed to the BCS by using the constant transformation matrix \mathbf{C}^{ij} which is the transformation matrix that defines the ICS orientation with respect to the BCS as discussed in Section 2.1. Therefore, the use of the ICS concept allows modeling different types of geometric discontinuities (T-, V-, and L-sections) in the FE mesh, while correctly representing the rigid body kinematics, inertia and dynamics.

3.2 ANCF Finite Elements

In case of ANCF elements, handling structural discontinuities requires the use of a fundamentally different approach that involves gradient transformations that have a structure different from the orthogonal vector transformations [31]. To this end, an appropriate coordinate transformation matrix that exists between the body and element parameterizations must be used, and no intermediate coordinate systems are required because of the use of the ANCF position vector gradients. The nodal coordinates defined with respect to the body parameterization can be transformed to coordinates with respect to the element parameterization as $\mathbf{e} = \mathbf{T}\mathbf{p}$, where \mathbf{e} and \mathbf{p} are the set of coordinates defined with respect to the element and body parameterizations, respectively, and the transformation \mathbf{T} can be written as

$$\mathbf{T} = \begin{bmatrix} \mathbf{I} & \mathbf{0} & \mathbf{0} & \mathbf{0} \\ \mathbf{0} & j_{1,1}\mathbf{I} & j_{2,1}\mathbf{I} & j_{3,1}\mathbf{I} \\ \mathbf{0} & j_{1,2}\mathbf{I} & j_{2,2}\mathbf{I} & j_{3,2}\mathbf{I} \\ \mathbf{0} & j_{1,3}\mathbf{I} & j_{2,3}\mathbf{I} & j_{3,3}\mathbf{I} \end{bmatrix} \quad (2)$$

where $j_{m,n} = \partial(\mathbf{S}_m \mathbf{e}_0) / \partial x_n$ are the components of the matrix of position vector gradients \mathbf{J}_0 defined at the reference configuration and \mathbf{S}_m is the m^{th} row of \mathbf{S} [31]. The transformation \mathbf{T} only affects the gradient vector coordinates of the given node, not the position vector coordinates. Employing this method, the structural discontinuities can be modeled using the conventional FE assembly procedure. By doing so, the connection between two ANCF elements having a structural discontinuity at a given common node is taken into account employing a standard connectivity matrix of the FE mesh. For example, consider the structure depicted in Fig. 5, which is the same as the one considered in the previous section. Without loss of generality, it is assumed that the BCS is parallel to the GCS. The structural discontinuity occurs at the shared node between the ANCF fully parameterized beam element 1 and element 2 as shown in Fig. 5. It can be seen from Fig. 5 that the orientation of the gradients in element 1 is the same as that of the BCS, whereas the

orientation of the gradients of element 2 is rotated with respect to the shown BCS. In this case, the transformation matrix that transforms the coordinates from the body to element parameterization will be an identity matrix at the shared node for element 1. For element 2, the transformation matrix will depend on the direction cosines between the gradients at the shared node in element 2 and the BCS assuming that the set of gradient vectors at the discontinuity node is an orthonormal set (no initial curvature). A similar procedure can be used for gradient deficient ANCF elements [32].

In this investigation, a new method for modeling structural discontinuities using ANCF elements is proposed. The proposed method generalizes the technique previously developed [31] to structural discontinuities located at arbitrary points of an FE/ANCF mesh. Instead of directly applying the coordinate transformation $\mathbf{e} = \mathbf{T}\mathbf{p}$ to switch to the body coordinates, a constant structural discontinuity constraint Jacobian matrix is defined. This Jacobian matrix can be used to define a constant velocity transformation matrix that can be used to systematically eliminate dependent variables. This approach offers the generality and flexibility of combining the structural discontinuity constraint equations with other constraint equations before switching to the body coordinates. By using this approach, structural discontinuities that occur at nodal locations of the FE/ANCF mesh can also be modeled, and therefore, the method previously developed in [31] can be considered as a special case of the method proposed in this section.

In the method proposed in this section, a set of ANCF structural discontinuity algebraic constraint equations is developed. Since these algebraic constraint equations are linear, they and the associated dependent variables can be systematically eliminated at a preprocessing stage, leading to reduced order models that can be efficiently solved. In order to obtain the general set of constraint equations associated with structural discontinuities, the proposed method is composed of two steps. In the first step, two sets of coordinate lines, which represent geometric lines

associated with the material fibers of the continuum body, are defined. The first set of coordinate lines referred to as $\bar{\mathbf{x}} = [\bar{x} \quad \bar{y} \quad \bar{z}]^T$ represents the element material fibers, whereas the second set of coordinate lines referred to as $\mathbf{x} = [x \quad y \quad z]^T$ represents the body material fibers. The set of coordinate lines \mathbf{x} are also referred to as *Cartesian coordinates* and serve as a unique standard for the FE mesh assembly, while the coordinate lines $\bar{\mathbf{x}}$ are simply referred to as *element coordinate lines*. Using these basic continuum mechanics concepts, the position field of a three-dimensional continuum body is defined as $\mathbf{r} = [r_1 \quad r_2 \quad r_3]^T$ and it can be written as a function of the element coordinate lines $\bar{\mathbf{x}}$ or as a function of the body coordinate lines \mathbf{x} . By using the chain rule of differentiation, one can write $(\partial \mathbf{r} / \partial \bar{\mathbf{x}}) = (\partial \mathbf{r} / \partial \mathbf{x})(\partial \mathbf{x} / \partial \bar{\mathbf{x}}) = (\partial \mathbf{r} / \partial \mathbf{x}) \mathbf{J}_b$, where \mathbf{J}_b is the Jacobian matrix that represents the transformation between the body coordinate lines and the element coordinate lines. Without loss of generality, the structural or body parameterization is defined considering the reference configuration of the continuum body, and therefore, the Jacobian matrix of the body parametrization \mathbf{J}_b is identical to the matrix of the position vector gradients \mathbf{J}_0 defined in the body reference configuration. This tensor transformation can be rewritten in matrix form as follows:

$$\begin{bmatrix} \mathbf{r}_{\bar{x}} & \mathbf{r}_{\bar{y}} & \mathbf{r}_{\bar{z}} \end{bmatrix} = \begin{bmatrix} \mathbf{r}_x & \mathbf{r}_y & \mathbf{r}_z \end{bmatrix} \mathbf{J}_0 = \begin{bmatrix} \mathbf{r}_x & \mathbf{r}_y & \mathbf{r}_z \end{bmatrix} \begin{bmatrix} j_{11} & j_{12} & j_{13} \\ j_{21} & j_{22} & j_{23} \\ j_{31} & j_{32} & j_{33} \end{bmatrix} \quad (3)$$

where $j_{m,n}$ are the components of the matrix \mathbf{J}_0 . By adding an identity transformation for the ANCF nodal position vector, the preceding equation can be rewritten as

$$\left. \begin{aligned} \mathbf{r} &= \mathbf{r} \\ \mathbf{r}_{\bar{x}} &= j_{11}\mathbf{r}_x + j_{21}\mathbf{r}_y + j_{31}\mathbf{r}_z \\ \mathbf{r}_{\bar{y}} &= j_{12}\mathbf{r}_x + j_{22}\mathbf{r}_y + j_{32}\mathbf{r}_z \\ \mathbf{r}_{\bar{z}} &= j_{13}\mathbf{r}_x + j_{23}\mathbf{r}_y + j_{33}\mathbf{r}_z \end{aligned} \right\} \quad (4)$$

For a general node of an ANCF fully-parameterized element, the nodal coordinate vector associated with the element coordinate lines can be defined as $\mathbf{e} = [\mathbf{r}^T \quad \mathbf{r}_{\bar{x}}^T \quad \mathbf{r}_{\bar{y}}^T \quad \mathbf{r}_{\bar{z}}^T]^T$, whereas the nodal coordinate vector associated with the structural (body) parametrization can be given by $\mathbf{p} = [\mathbf{r}^T \quad \mathbf{r}_x^T \quad \mathbf{r}_y^T \quad \mathbf{r}_z^T]^T$. Therefore, as mentioned before in this section, one can write $\mathbf{e} = \mathbf{T}\mathbf{p}$, where \mathbf{T} is the transformation matrix previously defined. On the other hand, the matrix of position vector gradients defined by differentiation with respect to the structural (body) parameters can be written as $(\partial\mathbf{r}/\partial\mathbf{x}) = (\partial\mathbf{r}/\partial\bar{\mathbf{x}})(\partial\bar{\mathbf{x}}/\partial\mathbf{x}) = (\partial\mathbf{r}/\partial\bar{\mathbf{x}})\mathbf{J}_b^{-1} = (\partial\mathbf{r}/\partial\bar{\mathbf{x}})\mathbf{H}_b$, where $\mathbf{H}_b = \mathbf{J}_b^{-1}$. Assuming again that the Jacobian matrix of the body parametrization \mathbf{J}_b is identical to the matrix of the position vector gradients \mathbf{J}_0 defined in the body reference configuration, this inverse tensor transformation can be rewritten in matrix form as follows:

$$\begin{bmatrix} \mathbf{r}_x & \mathbf{r}_y & \mathbf{r}_z \end{bmatrix} = \begin{bmatrix} \mathbf{r}_{\bar{x}} & \mathbf{r}_{\bar{y}} & \mathbf{r}_{\bar{z}} \end{bmatrix} \mathbf{H}_0 = \begin{bmatrix} \mathbf{r}_{\bar{x}} & \mathbf{r}_{\bar{y}} & \mathbf{r}_{\bar{z}} \end{bmatrix} \begin{bmatrix} h_{11} & h_{12} & h_{13} \\ h_{21} & h_{22} & h_{23} \\ h_{31} & h_{32} & h_{33} \end{bmatrix} \quad (5)$$

where $h_{m,n}$ are the components of the matrix $\mathbf{H}_0 = \mathbf{J}_0^{-1}$. It follows that

$$\left. \begin{aligned} \mathbf{r}_x &= h_{11}\mathbf{r}_{\bar{x}} + h_{21}\mathbf{r}_{\bar{y}} + h_{31}\mathbf{r}_{\bar{z}} = (h_{11}\mathbf{S}_{\bar{x}} + h_{21}\mathbf{S}_{\bar{y}} + h_{31}\mathbf{S}_{\bar{z}})\mathbf{e} = \mathbf{S}_x\mathbf{T}\mathbf{p} \\ \mathbf{r}_y &= h_{12}\mathbf{r}_{\bar{x}} + h_{22}\mathbf{r}_{\bar{y}} + h_{32}\mathbf{r}_{\bar{z}} = (h_{12}\mathbf{S}_{\bar{x}} + h_{22}\mathbf{S}_{\bar{y}} + h_{32}\mathbf{S}_{\bar{z}})\mathbf{e} = \mathbf{S}_y\mathbf{T}\mathbf{p} \\ \mathbf{r}_z &= h_{13}\mathbf{r}_{\bar{x}} + h_{23}\mathbf{r}_{\bar{y}} + h_{33}\mathbf{r}_{\bar{z}} = (h_{13}\mathbf{S}_{\bar{x}} + h_{23}\mathbf{S}_{\bar{y}} + h_{33}\mathbf{S}_{\bar{z}})\mathbf{e} = \mathbf{S}_z\mathbf{T}\mathbf{p} \end{aligned} \right\} \quad (6)$$

where $\mathbf{S}_x = (h_{11}\mathbf{S}_{\bar{x}} + h_{21}\mathbf{S}_{\bar{y}} + h_{31}\mathbf{S}_{\bar{z}})$, $\mathbf{S}_y = (h_{12}\mathbf{S}_{\bar{x}} + h_{22}\mathbf{S}_{\bar{y}} + h_{32}\mathbf{S}_{\bar{z}})$, and $\mathbf{S}_z = (h_{13}\mathbf{S}_{\bar{x}} + h_{23}\mathbf{S}_{\bar{y}} + h_{33}\mathbf{S}_{\bar{z}})$.

By using these equations, one is able to write the gradient vectors of a given ANCF element as

functions of the structural (body) vector of nodal coordinates. Therefore, considering two material points P^i and P^j belonging to the element i and j , respectively, one can write a set of structural discontinuity constraint equations for the connection of points P^i and P^j as follows:

$$\left. \begin{aligned} \mathbf{r}^i(P^i) - \mathbf{r}^j(P^j) &= \mathbf{0}, & \mathbf{r}_x^i(P^i) - \mathbf{r}_x^j(P^j) &= \mathbf{0}, \\ \mathbf{r}_y^i(P^i) - \mathbf{r}_y^j(P^j) &= \mathbf{0}, & \mathbf{r}_z^i(P^i) - \mathbf{r}_z^j(P^j) &= \mathbf{0} \end{aligned} \right\} \quad (7)$$

or equivalently

$$\left. \begin{aligned} \mathbf{S}^i \mathbf{T}^i \mathbf{p}^i - \mathbf{S}^j \mathbf{T}^j \mathbf{p}^j &= \mathbf{0}, & \mathbf{S}_x^i \mathbf{T}^i \mathbf{p}^i - \mathbf{S}_x^j \mathbf{T}^j \mathbf{p}^j &= \mathbf{0}, \\ \mathbf{S}_y^i \mathbf{T}^i \mathbf{p}^i - \mathbf{S}_y^j \mathbf{T}^j \mathbf{p}^j &= \mathbf{0}, & \mathbf{S}_z^i \mathbf{T}^i \mathbf{p}^i - \mathbf{S}_z^j \mathbf{T}^j \mathbf{p}^j &= \mathbf{0} \end{aligned} \right\} \quad (8)$$

Considering the vector of structural nodal coordinates $\mathbf{p}^k = \left[(\mathbf{p}^i)^T \quad (\mathbf{p}^j)^T \right]^T$ that appears in the preceding equation, the structural discontinuity constraint Jacobian matrix can be written as

$$\mathbf{C}_{\mathbf{p}^k}^k = \begin{bmatrix} \mathbf{C}_{\mathbf{p}^i}^k & \mathbf{C}_{\mathbf{p}^j}^k \end{bmatrix} = \begin{bmatrix} \mathbf{S}^i \mathbf{T}^i & -\mathbf{S}^j \mathbf{T}^j \\ \mathbf{S}_x^i \mathbf{T}^i & -\mathbf{S}_x^j \mathbf{T}^j \\ \mathbf{S}_y^i \mathbf{T}^i & -\mathbf{S}_y^j \mathbf{T}^j \\ \mathbf{S}_z^i \mathbf{T}^i & -\mathbf{S}_z^j \mathbf{T}^j \end{bmatrix} \quad (9)$$

where \mathbf{C}^k denotes the vector of structural discontinuity constraint equations of Eq. 7 and 8 at node k . Since the structural discontinuity constraint equations are a set of linear algebraic equations grouped in the vector \mathbf{C}^k , the Jacobian matrix $\mathbf{C}_{\mathbf{p}^k}^k$ of this set of algebraic equations is constant, and therefore, the constraint equations and the associated dependent variables can be systematically eliminated at a preprocessing stage by developing an appropriate velocity transformation matrix. The use of the velocity transformation matrix offers the flexibility and generality of combining the structural discontinuity constraint equations with other constraint equations which are formulated in terms of the original element nodal coordinates.

4. MBS EQUATIONS OF MOTION

The equations of motion used in this investigation for the dynamic simulation of a vehicle system that consists of rigid, FE/FFR, and ANCF bodies are presented in this section. The differential/algebraic equations of motion are obtained using the principle of virtual work and the technique of Lagrange multipliers. The set of generalized coordinates used are $\mathbf{q} = [\mathbf{q}_r^T \quad \mathbf{q}_f^T \quad \mathbf{p}^T]^T$, where $\mathbf{q}_r = [\mathbf{q}_R^T \quad \mathbf{q}_\theta^T]^T$ are the rigid body translational and rotational coordinates collectively referred to as reference coordinates, \mathbf{q}_f represents the FE/FFR coordinates, and \mathbf{p} represents the vector of structural FE/ANCF coordinates. The equations of motion used in this study can be written as

$$\begin{bmatrix} \mathbf{M}_{rr} & \mathbf{M}_{rf} & \mathbf{0} & \mathbf{C}_{q_r}^T \\ \mathbf{M}_{fr} & \mathbf{M}_{ff} & \mathbf{0} & \mathbf{C}_{q_f}^T \\ \mathbf{0} & \mathbf{0} & \mathbf{M}_{pp} & \mathbf{C}_p^T \\ \mathbf{C}_{q_r} & \mathbf{C}_{q_f} & \mathbf{C}_p & \mathbf{0} \end{bmatrix} \begin{bmatrix} \ddot{\mathbf{q}}_r \\ \ddot{\mathbf{q}}_f \\ \ddot{\mathbf{p}} \\ \lambda \end{bmatrix} = \begin{bmatrix} \mathbf{Q}_r + \mathbf{Q}_{v_r} \\ \mathbf{Q}_f + \mathbf{Q}_{v_f} \\ \mathbf{Q}_e \\ \mathbf{Q}_c \end{bmatrix} \quad (10)$$

where \mathbf{M}_{rr} and \mathbf{M}_{ff} are the mass matrices associated with the reference and FE/FFR deformation coordinates, respectively; \mathbf{M}_{rf} and \mathbf{M}_{fr} represent the inertia coupling between the FE/FFR reference and deformation coordinates; \mathbf{M}_{pp} is the mass matrix associated with the ANCF coordinates; \mathbf{C}_{q_r} , \mathbf{C}_{q_f} , and \mathbf{C}_p are the Jacobian matrices of the nonlinear MBS joint constraint equations associated, respectively, with the reference, FE/FFR deformation, and ANCF coordinates; λ is the vector of Lagrange multipliers; \mathbf{Q}_r , \mathbf{Q}_f , and \mathbf{Q}_e are the applied and elastic force vectors associated with the reference, FE/FFR deformation, and ANCF coordinates respectively; \mathbf{Q}_{v_r} and \mathbf{Q}_{v_f} are the Coriolis and centrifugal force vectors associated with the

reference and FE/FFR deformation coordinates, respectively; and \mathbf{Q}_c is the quadratic velocity vector that arises from differentiating the constraint equations twice with respect to time.

For numerically solving the equations of motion, the *two-loop implicit sparse matrix numerical integration* (TLISMNI) method that utilizes the concept of coordinate partitioning and the second-order backward difference formula for time integration is used in this work [33]. An important feature of TLISMNI is that it satisfies the constraint equations at the position, velocity, and acceleration levels. A component mode synthesis method is used for the FE/FFR model to reduce the size of the modal transformation matrix by eliminating insignificant high frequency modes. Furthermore, the concept of the *ANCF reference node* is used to model the rigid rim in the ANCF tire assembly. Using the ANCF reference node, linear constraint equations can be formulated for the tire-rim connection and the dependent variables in the tire mesh can then be eliminated thus reducing the model dimensionality and the number of Lagrange multipliers needed in the dynamic analysis [4, 18]. The rigidity of the ANCF reference node is ensured by imposing six nonlinear constraint equations that ensure that its gradient vectors remain unit orthogonal vectors in order to define an orthonormal rigid body coordinate system.

5. NUMERICAL RESULTS AND DISCUSSION

This section presents and discusses two simple ANCF pendulum problems and a complex off-road vehicle model that includes flexible ANCF tires and FE/FFR chassis in order to demonstrate the use of the new velocity transformation-based approach introduced in Section 3.2 for modeling structural discontinuities in the analysis of a complex vehicle model with flexible chassis and tires without the need for co-simulation.

5.1 L-shaped Beam and Y-shaped Plate Pendulums

In order to demonstrate the implementation of the new ANCF approach discussed in Section 3.2 for modeling structural discontinuities, beam and plate pendulum models are used in this section. The beam model, which is an L-shaped pendulum model shown in Fig. 6, consists of two ANCF fully parameterized beam elements that are connected at a structural discontinuity node. Three beam pendulum models are considered in this numerical study: rigid body, ANCF with modulus of elasticity $E = 2 \times 10^{12}$ Pa, and ANCF with modulus of elasticity $E = 2 \times 10^7$ Pa. The length, width, and height of the beams are 1m, 0.1m, and 0.1m, respectively. A density $\rho = 1000$ kg/m³ and Poisson's ratio $\nu = 0$ are assumed. Figure 7 shows the time evolution of the pendulum tip vertical position for the three models. As can be seen from Fig. 7, the rigid body and stiff ANCF pendulum models are overlapping, whereas there is some difference in the results of the soft ANCF pendulum model. The soft ANCF pendulum, however, follows a similar trend as that exhibited by the other two models. In order to examine the results of the new implementation, Fig. 8 compares two scalar quantities and their difference at the structural discontinuity node of the ANCF model with $E = 2 \times 10^7$ Pa. These scalar quantities are $\mathbf{r}_{x1}^T \mathbf{r}_{x2}$ and $\mathbf{r}_{x1}^T \mathbf{r}_{z1}$, where the subscript $\alpha\beta$ refers to the α coordinate line on element β . The scalar quantity $\mathbf{r}_{x1}^T \mathbf{r}_{x2}$ corresponds approximately to the cosine of the angle between the two beams, whereas $\mathbf{r}_{x1}^T \mathbf{r}_{z1}$ corresponds to the engineering shear strain at the structural discontinuity node. It is shown in Fig. 8 that $\mathbf{r}_{x1}^T \mathbf{r}_{x2}$ and $\mathbf{r}_{x1}^T \mathbf{r}_{z1}$ overlap and their difference is identically zero throughout the simulation.

The plate/shell model consists of three fully parameterized ANCF plate/shell elements connecting at common structural discontinuity nodes and making a Y-shaped plate structure as shown in Fig. 9. The two angled plates connect to the horizontal plate at a 45° angle measured from the horizontal plane. Figure 10 compares the right tip vertical position of the upper angled

plate of a rigid body model to an ANCF model with $E = 2 \times 10^{12}$ Pa. The length, width and height of the plates are 1m, 1m, and 0.1m respectively. A density $\rho = 1000$ kg/m³ and Poisson's ratio $\nu = 0$ are used for the ANCF plate pendulum. As can be seen from Fig. 10, even in this case, the rigid body and stiff ANCF pendulum models produce the same results, thus demonstrating the effectiveness of the proposed ANCF approach for modeling structural discontinuities.

5.2 Wheeled Vehicle Model

An off-road four-wheel drive vehicle model, HMMWV model shown in Fig. 11, is considered as a numerical example in this section. A MBS model with a detailed suspension model was developed. The chassis and tires are considered flexible bodies in this MBS vehicle model. The chassis is modeled using the FE/FFR formulation whereas the tires are modeled using ANCF elements. Two types of flexible tires that include a pneumatic tire and an airless (non-pneumatic) tire are considered and the results obtained using these distributed inertia and elasticity tire models are compared with a rigid brush-type tire model.

5.2.1 MBS Vehicle Model

The vehicle model considered in this numerical study is a four-wheel drive vehicle capable of operating both on-road and off-road. The vehicle has a 190-horsepower engine, a double 'A' arm suspension with coil springs and double-acting shock absorbers and a recirculating ball, worm and nut based power assisted steering. The gross operating mass of the vehicle can vary, however, a good estimate of the vehicle curb mass is approximately 2500 kg. The maximum vehicle on-road speed is around 113 km/h. For simplicity, powertrain dynamics are not considered in the MBS model used in this numerical study. The steering system is modeled using a rack-pinion system. The vehicle subsystems like suspension, car-body, chassis, and tires are modeled in detail using several rigid and deformable bodies. Table 1 shows the body inertia of the vehicle components,

whereas Tables 2 and 3 show the different types of ideal and compliant joints used in the model. Figure 12 shows a detailed view of the suspension system and some driveline components used in this model. Three different types of tires are used with the model, these include rigid brush-type tire, FE/ANCF pneumatic tire, and FE/ANCF airless tire. The computer implementation of the new approach proposed in this study in Section 3 for the treatment of the structural discontinuities was used in the analysis of the ANCF airless tire model developed in this study.

For the assembly of the vehicle model, four subsystems are considered: car body, chassis, suspension, and wheels. The wheels are connected to the spindles (suspension component) using revolute joints and the spindles are connected to the upright using revolute joints. A component called the subframe connects the suspension, chassis and car body. The chassis is connected to the front and rear subframes at the NDRC locations shown in Fig. 13 using bearing elements. In this paper, NDRC is an abbreviation for **n**odal **d**isplacement **r**eference **c**onditions, which refer to the locations on the chassis where the node displacements are constrained in order to achieve a unique displacement field for the FE/FFR chassis mesh. Furthermore, the car body is also connected to the sub-frames at the same locations as that of the chassis using bearing elements. The upper and lower arms of the suspension shown in Fig. 12 are connected to their respective sub-frame using revolute joints.

5.2.2 Flexible Subsystems: Chassis and Tires

The FE/FFR method is used to model the vehicle chassis which is meshed using 435 non-isoparametric three-dimensional beam elements with displacement and rotations as nodal coordinates. The shape function matrix for this non-isoparametric beam element is given in Appendix A.1. The material parameters considered are modulus of elasticity $E = 2.1 \times 10^{11}$ Pa, Poisson ratio $\nu = 0.33$, and mass density $\rho = 7200$ kg/m³. The cross-section is assumed to be

rectangular with width $w = 0.05$ m and height $h = 0.1$ m. The FE mesh and the applied reference conditions are shown in Fig. 13. As shown in this figure, the reference conditions are selected to constrain the x , y and z nodal displacement at 8 nodes/points which represent joints between the vehicle suspension subsystem and chassis. The dimension of the chassis model is reduced by eliminating high-frequency modes and keeping the first 15 modes in the model. Modal damping is used in order to account for the dissipation due to structural damping. A damping ratio of 1% is used for the first 5 modes and a damping ratio of 5% is used on the remaining higher frequency modes in order to damp out insignificant high-frequency oscillations and improve the computational efficiency of the model. The first five modes of the chassis are shown in Fig. 14, while Table 4 shows the frequencies associated with the 15 modes of the chassis.

ANCF fully-parameterized plate/shell elements, on the other hand, are used to model the pneumatic and airless tires. One of the tires in the 144-element pneumatic four-tire mesh is shown in Fig. 15, while one of the tires in the 100-element airless four-tire mesh is shown in Fig. 16. The linear isotropic material properties selected are $\rho = 1500$ kg/m³, $E = 5 \times 10^7$ Pa, and $\nu = 0$. For simplicity viscoelasticity was not considered in this study, however dissipative forces were added to the tire using a discrete damping model described in the next paragraph. The air-pressure considered in the pneumatic tire is 250 kPa. The tire/ground contact penalty stiffness, damping, and coulomb friction coefficients are selected to be $k = 5 \times 10^4$ N/m, $c = 4 \times 10^3$ N.s/m, and $\mu = 0.8$, respectively. More details on the ANCF tire/ground contact formulation can be found in the investigation by Patel et al. [4].

Finally, a new radial damping model for the tire is introduced wherein the relative velocity between the tire material point and the ANCF reference node that is used to model the rim is used in the formulation of the damping force as shown in Fig. 17. This type of damping is introduced

in the model to simulate the effect of the more realistic material damping that would occur in the tire structure. However, using this type of damping, one can relate the damping coefficient to radial damping used in several non-FE based ring type tire models which are parametrized using test data. The relative velocity between the tire material point and the ANCF reference node, \mathbf{v}_r , is calculated and its projection on the outward normal to the tire surface at that material point is used in the damping force expression. Hence, the generalized damping forces can be written as $\mathbf{Q}_d = -\int_s \mathbf{S}^T c(\mathbf{v}_r^T \mathbf{n}) \mathbf{n} ds$, where c is a damping coefficient, \mathbf{S} is the matrix of shape functions, \mathbf{n} is the outward normal to the tire surface as shown in Fig. 17, and s is the tire surface area. The generalized damping forces used in this investigation are distributed forces calculated from integration over the tire surface area. Furthermore, this damping formulation does not affect the ability of the ANCF mesh to correctly exhibit rigid body motion since the relative velocity of the material point with respect to the ANCF rim node instead of its absolute velocity is used in the formulation of the damping force. The tire edges are clamped to the rim using linear constraints at the preprocessing stage, hence removing any rigid body motion between the tire and its respective rim reference node [18]. A damping coefficient of $c = 2 \times 10^4 \text{ N.s/m}$ was used with the pneumatic tire model in this study. Adding the damping to the tire model significantly improved its computational efficiency and improved the quality of the results leading to a more realistic behavior.

5.2.3 Comparative Study

In order to compare the response of different tire models considered in this study as well as the vehicle response, the off-road wheeled vehicle model described in Section 5.2.1 is made to traverse several curb-like bumps. The three vehicle models used in this analysis have the same kinematic constraints and model topology. The models with the airless ANCF tire, pneumatic ANCF tire,

and brush tire will be henceforth referred to as airless, pneumatic, and brush models respectively. Table 5 shows the brush tire parameters used with the brush tire vehicle model. The topology of the test track, shown in Fig. 18, can be used to assess vehicle durability and study the noise-vibration-harshness (NVH) response of the vehicle. The vehicle is allowed to settle initially, and then driving moments are applied to the wheels from 0.5s to 8.5s, after which the driving moments are removed and the vehicle is allowed to decelerate. The vehicle reaches a maximum velocity of around 17 km/h during the 15s simulation. Figure 19 shows the chassis longitudinal velocity of the three vehicle models. Figure 20 shows the chassis longitudinal displacement of the three vehicle models. There are some differences in the vehicle longitudinal displacement due to the different rolling resistance coefficients of the tires that are in turn dependent on the tire geometry and the resulting contact patch as well as the normal contact force distribution. Figure 21 shows the vertical displacement of the chassis reference. It can be noted from Fig. 21 that, objectively, the motion of the chassis frame of reference is quite similar for all three tire models. The chassis vertical displacement for the brush tire model is slightly larger than the FE/ANCF tire models at certain time points since the brush tire model is based on a rigid tire assumption with a flexible contact patch, and leads to larger force transmission, hence slightly larger vibration amplitude of the chassis which is modeled as a sprung mass. Figure 22 shows the vertical displacement of the front left spindle as the suspension subsystems traverse the seven curb-like bumps in the test track. It can be noted from Fig. 22 that the upward displacement due to a bump in case of the brush tire model occurs with a slight delay when compared to that of the FE/ANCF tire models. The reason for this phenomenon is that the brush tire model has a single contact point directly below the wheel center, hence the bump is only detected by the brush tire model when the brush tire center coincides with the start of the bump. In case of the FE/ANCF tires, since the contact detection is done for

the elements near the ground while accounting for the variation in the ground geometry due to the bumps, the FE tires can detect the sudden change in ground geometry away from wheel center with much higher accuracy than the brush tire model. However, it must be noted that the brush tire model is typically used in ride quality simulations instead of NVH-type durability simulations. Figures 23 and 24 show the strains in the front right airless and pneumatic tires as they come into contact with the second bump of the test track, respectively. Along with examining the dynamic events occurring in the flexible tires, the chassis that is modeled using the FE/FFR approach can be analyzed for deformation and stress hot spots in order to improve its design or simply ensure that stresses remain within the material yield limit when the model is tested under certain external excitations and loads. Figure 25 shows the chassis total deformation for the dynamic event of the vehicle front tires passing over the second bump. Figure 26 shows the vertical deformation time history of point P shown in Fig. 25. Since the deformation data shown in Fig. 26 contain some high frequencies, it can be harder to correlate it with the vehicle overall motion, for this reason, Fig. 27 shows the vertical deformation of chassis point P after applying a low-pass filter with a cut-off frequency of 3.33 Hz. Similar to analyzing the deformations, element stresses can also be extracted and analyzed. Figure 28 shows the axial stress at point P whereas Fig. 29 shows the same result after applying the low-pass filter. It can be seen from the results of Figs. 26-29 that the chassis vertical deformation and axial stress for the three types of tire models traversing the test track is quite similar. The deformation in the chassis used with brush tire model is larger than its FE/ANCF counterparts due to the reason previously mentioned, that is, the rigidity of the tire which leads to larger force transmission.

Figure 30 shows the front left spindle vertical forces as a function of its longitudinal displacement. The spindle force refers to the upright reaction force acting on the spindle in the

spindle-upright revolute joint. Appendix B briefly discusses the constraint force calculations based on the MBS approach adopted in this investigation. It can be noted from the results presented in Fig. 30 that the brush tire has high force spikes compared to the pneumatic and airless tires. Figure 31 shows a zoomed in view of Fig. 30 in the 10-15 m displacement segment. It can be seen that even in transient events, the spindle forces of all three types of tires can follow a very similar pattern. There are, however, two large force spikes in case of the brush tire model in Fig. 31 which occur with a slight delay when compared to the airless and pneumatic tire models. These force spikes occur when the tires come into contact with the bumps. As mentioned previously, due to the differences in how the brush tire and ANCF tires models handle contact, there will be difference in the dynamic response in the neighborhood of the beginning of the bumps. Figures 32 and 33 show the spindle longitudinal and lateral force, respectively. The spindle forces shown in Figs. 30 - 33 are given with respect to the global reference frame. The high frequency spindle joint reaction force content seen in case of the airless tire can be attributed to the fact that no material damping was considered. Material damping can be introduced for the ANCF tire models by accounting for the viscoelastic properties that will be considered in future studies.

It must be noted that even though this is a comparison study of different types of tires and their simulation-based models, the tire models considered are based on different parameters or inputs that must be accurately determined. The fidelity of the FE-based tire models, including the airless and pneumatic tires, is dependent on the geometric and material properties and complexities considered in the FE modeling of these tires. The brush tire model on the other hand uses specific inputs such as radial, longitudinal slip, and lateral slip stiffness parameters in addition to some other tire properties like rolling resistance and friction coefficients. Because of the difficulties of obtaining data from tire manufacturers and because this study is mainly concerned with

demonstrating how structural discontinuities using large and small deformation formulations can be incorporated in the flexible MBS model, the brush tire parameters were varied until the model yielded similar global motion trajectories as those of the FE models. For a detailed comparison, ideally, the brush tire parameters must be optimized to match experimental data or simulation data that were previously verified numerically. Such optimization can be done iteratively or through optimization algorithms as was demonstrated by Li et al. [34].

6 SUMMARY AND CONCLUSIONS

The goal of this investigation is to develop a computational framework for complex vehicle systems that consist of components with geometry characterized by structural discontinuities as in the cases of chassis and airless tires. Accurate durability analysis of such systems requires the integration of small- and large-deformation formulations. The paper proposes a new ANCF approach for modeling structural discontinuities in which a constant velocity transformation matrix that allows combining the structural discontinuity constraint equations with other ANCF constraint equations before the application of any coordinate transformation. The ANCF linear constraint equations are used to eliminate dependent variables at a preprocessing stage. The paper also proposes a new radial damping model for the tires and demonstrates its use in MBS vehicle system applications. The use of the new computational framework proposed in this study is demonstrated by developing and performing the simulation of a detailed wheeled vehicle model that consists of rigid body, FFR, and ANCF components. The vehicle components undergoing small deformations are modeled using the FFR approach, whereas the components undergoing large deformations and finite rotations are modeled using the ANCF approach. Three types of tire models that include a rigid brush-type tire model, an ANCF airless tire model, and an ANCF pneumatic tire model are

compared as the vehicle traverses a series of bumps. The airless tire is modeled for the first time using ANCF fully parameterized plate/shell elements, which is one of the main contributions of this investigation.

APPENDIX A

A.1 FE/FFR Beam Element Shape Function Matrix

The shape function matrix for the non-isoparametric beam element used with the FE/FFR model in this investigation is given as

$$\mathbf{S}^{ijT} = \begin{bmatrix} 1-\xi & 0 & 0 \\ 6(\xi-\xi^2)\eta & 1-3\xi^2+2\xi^3 & 0 \\ 6(\xi-\xi^2)\zeta & 0 & 1-3\xi^2+2\xi^3 \\ 0 & -(1-\xi)l\zeta & (1-\xi)l\eta \\ (1-4\xi+3\xi^2)l\zeta & 0 & (-\xi+2\xi^2-\xi^3)l \\ (-1+4\xi-3\xi^2)l\eta & (\xi-2\xi^2+\xi^3)l & 0 \\ \xi & 0 & 0 \\ 6(-\xi+\xi^2)\eta & 3\xi^2-2\xi^3 & 0 \\ 6(-\xi+\xi^2)\zeta & 0 & 3\xi^2-2\xi^3 \\ 0 & -l\xi\zeta & l\xi\eta \\ (-2\xi+3\xi^2)l\zeta & 0 & (\xi^2-\xi^3)l \\ (2\xi-3\xi^2)l\eta & (-\xi^2+\xi^3)l & 0 \end{bmatrix} \quad (\text{A.1})$$

A.2 ANCF Plate/Shell Element Shape Functions

The shape function matrix and the shape functions of the ANCF fully-parameterized plate/shell element with gradient conformity at element edges are given, respectively, as

$$\mathbf{S} = [\mathbf{S}_1 \mathbf{I} \quad \mathbf{S}_2 \mathbf{I} \quad \mathbf{S}_3 \mathbf{I} \quad \mathbf{S}_4 \mathbf{I} \quad \mathbf{S}_5 \mathbf{I} \quad \mathbf{S}_6 \mathbf{I} \quad \mathbf{S}_7 \mathbf{I} \quad \mathbf{S}_8 \mathbf{I} \quad \mathbf{S}_9 \mathbf{I} \quad \mathbf{S}_{10} \mathbf{I} \quad \mathbf{S}_{11} \mathbf{I} \quad \mathbf{S}_{12} \mathbf{I} \quad \mathbf{S}_{13} \mathbf{I} \quad \mathbf{S}_{14} \mathbf{I} \quad \mathbf{S}_{15} \mathbf{I} \quad \mathbf{S}_{16} \mathbf{I}] \quad (\text{A.2})$$

and

$$\left. \begin{aligned}
S_1 &= (2\xi + 1)(\xi - 1)^2 (2\eta + 1)(\eta - 1)^2 \quad ; \quad S_2 = l\xi(\xi - 1)^2 (2\eta + 1)(\eta - 1)^2 \\
S_3 &= w\eta(\xi - 1)^2 (2\xi + 1)(\eta - 1)^2 \quad ; \quad S_4 = t\zeta(\xi - 1)(\eta - 1) \\
S_5 &= -\xi^2 (2\xi - 3)(2\eta + 1)(\eta - 1)^2 \quad ; \quad S_6 = l\xi^2 (\xi - 1)(2\eta + 1)(\eta - 1)^2 \\
S_7 &= -w\eta\xi^2 (2\xi - 3)(\eta - 1)^2 \quad ; \quad S_8 = -t\xi\zeta(\eta - 1) \\
S_9 &= \eta^2 \xi^2 (2\xi - 3)(2\eta - 3) \quad ; \quad S_{10} = -l\eta^2 \xi^2 (\xi - 1)(2\eta - 3) \\
S_{11} &= -w\eta^2 \xi^2 (\eta - 1)(2\xi - 3) \quad ; \quad S_{12} = t\zeta\xi\eta \\
S_{13} &= -\eta^2 (2\xi + 1)(\xi - 1)^2 (2\eta - 3) \quad ; \quad S_{14} = -l\xi\eta^2 (\xi - 1)^2 (2\eta - 3) \\
S_{15} &= w\eta^2 (\xi - 1)^2 (2\xi + 1)(\eta - 1) \quad ; \quad S_{16} = -t\zeta\eta(\xi - 1)
\end{aligned} \right\} \quad (A.3)$$

where $\xi = x/l$, $\eta = y/w$, and $\zeta = z/t$ in which l , w , and t are, respectively, the length, width, and thickness of the plate.

APPENDIX B

Joint Reaction Force Calculation

The reaction forces for a given joint can be calculated using the Lagrange multipliers and the constraint Jacobian matrix, shown in Eq. 10. The generalized constraint forces can be written as $\mathbf{Q}_c = -\mathbf{C}_q^T \boldsymbol{\lambda}$, where \mathbf{C}_q represents the Jacobian matrix associated with the joint and $\boldsymbol{\lambda}$ is the vector of Lagrange multipliers associated with the joint which are solved for along with the accelerations in Eq. 10.

In case of a revolute joint which connects the spindle and upright, the kinematic constraints can be written as [35]

$$\mathbf{C} = \begin{bmatrix} \mathbf{r}_p^i - \mathbf{r}_p^j \\ \mathbf{v}_1^{iT} \mathbf{v}^j \\ \mathbf{v}_2^{iT} \mathbf{v}^j \end{bmatrix} \quad (\text{B.1})$$

where superscripts refer to the two bodies connected by the joint, P is the joint definition point, \mathbf{v}^i and \mathbf{v}^j are vectors along the joint axis, \mathbf{v}_1^i and \mathbf{v}_2^i are vectors that make an orthonormal triad along with \mathbf{v}^i . Using the preceding equation, the Jacobian matrix for the revolute joint can be written as

$$\mathbf{C}_q = \begin{bmatrix} \mathbf{H}_p^i & -\mathbf{H}_p^j \\ \mathbf{v}^{jT} \mathbf{L}_1^i & \mathbf{v}_1^{iT} \mathbf{L}^j \\ \mathbf{v}^{jT} \mathbf{L}_2^i & \mathbf{v}_2^{iT} \mathbf{L}^j \end{bmatrix} \quad (\text{B.2})$$

where $\mathbf{H}_p^k = \begin{bmatrix} \mathbf{I} & \mathbf{A}^k \tilde{\mathbf{u}}_p^{kT} \bar{\mathbf{G}}^k \end{bmatrix}$ for $k = i, j$, \mathbf{A} is the body transformation matrix, $\tilde{\mathbf{u}}_p$ is the vector that defines the position of the joint definition point with respect to the body coordinate system, $\bar{\mathbf{G}}$ is the matrix that relates the body orientation parameter time derivatives to the angular velocity vector $\bar{\boldsymbol{\omega}}$ defined in the body coordinate system, and $\mathbf{L}_m^k = \mathbf{A}^k \tilde{\mathbf{v}}_m^{kT} \bar{\mathbf{G}}^k$ for $k = i, j$ and $m = 1, 2$ [35].

REFERENCES

1. Orlandea, N., 1973, "Node-analogous, Sparsity-oriented Methods for Simulation of Mechanical Dynamic Systems," Ph.D. Thesis, University of Michigan, Ann Arbor.
2. Wehage, R.A., Haug, E.J., Barman, N.C., and Beck, R.R., 1981, "Dynamic Analysis and Design of Constrained Mechanical Systems," Technical Report No. 50, Contract No. DAAK30-78-C-0096.
3. Shabana, A.A., 2013, *Dynamics of Multibody Systems*, 4th Edition, Cambridge University Press, Cambridge.
4. Patel, M., Orzechowski, G., Tian, Q., and Shabana, A.A., 2016, "A New Multibody Approach for Tire Modeling using ANCF Finite Elements," *Proc. Of IMechE Part K: Journal of Multibody Dynamics*, 230(1), pp. 69-84.
5. Recuero, A., Contreras, U., Patel, M., and Shabana, A.A., 2016, "ANCF Continuum-based Soil Plasticity for Wheeled Vehicle Off-road Mobility," *ASME Journal of Computational and Nonlinear Dynamics*, 11, 044504-1 – 044504-5.
6. Shabana, A.A., 2018, *Computational Continuum Mechanics*, 3rd Edition, Cambridge University Press, Cambridge.
7. Blundell, M., and Harty, D., 2004, *Multibody Systems Approach to Vehicle Dynamics*, Elsevier, New York.
8. Shabana, A.A., 1985, "Substructure Synthesis Methods for Dynamic Analysis of Multibody Systems," *Computers and Structures*, 20(4), pp. 737-744.
9. Agrawal, O.P., and Shabana, A.A., 1986, "Application of Deformable-Body Mean Axis to Flexible Multibody System Dynamics," *Computer Methods in Applied Mechanics and Engineering*, 56, pp. 217-245.

10. Ambrosio, J.A.C, and Goncalves, J.P.C., 2001, "Complex Flexible Multibody Systems with Application to Vehicle Dynamics," *Multibody System Dynamics*, 6, pp. 163-182.
11. Sampo, E., 2010, "Modelling Chassis Flexibility in Vehicle Dynamics Simulation," Ph.D. Thesis, University of Surrey, Surrey.
12. Shiiba, T., Fehr, J., and Eberhard, P., 2012, "Flexible Multibody Simulation of Automotive Systems with Non-modal Model Reduction Techniques," *Vehicle System Dynamics*, 50(12), pp. 1905-1922.
13. Carpinelli, M., Mundo, D., Tamarozzi, T., Gubitosa, M., Donders, S., and Desmet, W., 2012, "Integrating Vehicle Body Model Concept Modelling and Flexible Multibody Techniques for Ride and Handling Simulation," *Proc. Of ASME 11th Biennial Conference on Engineering Systems Design and Analysis*, Nantes, France, July 2-4 2012.
14. Goncalves, J.P.C., and Ambrosio, J.A.C., 2003, "Optimization of Vehicle Suspension Systems for Improved Comfort of Road Vehicles using Flexible Multibody Dynamics," *Nonlinear Dynamics*, 34, pp. 113-131.
15. Pacejka, H. B., 2002, *Tire and Vehicle Dynamics*, Society of Automotive Engineers (SAE), Warrendale, PA.
16. Gipser, M., 2005, "FTire: A Physically Based Application-Oriented Tyre Model for Use with Detailed MBS and Finite-Element Suspension Models", *Vehicle System Dynamics*, Vol. 43, pp. 76-91.
17. Koishi, M., Kabe, K. and Shiratori, M., 1998, "Tire Cornering Simulation Using an Explicit Finite Element Analysis Code", *Tire Science and Technology*, Vol. 26, pp. 109-119.
18. Shabana, A.A., 2015, "ANCF Tire Assembly Model for Multibody System Applications", *ASME Journal of Computational and Nonlinear Dynamics*, 10(2), 024504-1 - 024504-4.

19. Pappalardo, C. M., Yu, Z., Zhang, X., and Shabana, A. A., 2016, "Rational ANCF Thin Plate Finite Element", *ASME Journal of Computational and Nonlinear Dynamics*, 11(5), 051009.
20. Pappalardo, C. M., Wallin, M., and Shabana, A. A., 2016, "A New ANCF/CRBF Fully Parametrized Plate Finite Element," *ASME Journal of Computational and Nonlinear Dynamics*, 12(3), pp. 1-13.
21. Yamashita, H., Jayakumar, P. and Sugiyama, H., 2016, "Physics-based Flexible Tire Model Integrated with LuGre Tire Friction for Transient Braking and Cornering Analysis," *ASME Journal of Computational and Nonlinear Dynamics*, 11(3), 031017-1 – 031017-17.
22. Sugiyama, H., and Suda, Y., 2009, "Nonlinear Elastic Ring Tyre Model using the Absolute Nodal Coordinate Formulation," *Proc. Of IMechE Part K: Journal of Multibody Dynamics*, 223(3), pp. 211-219.
23. Recuero, A., Serban, R., Peterson, B., Sugiyama, H., Jayakumar, P., and Negrut, D., 2017, "A High-fidelity Approach for Vehicle Mobility Simulation: Nonlinear Finite Element Tires Operating on Granular Material," *Journal of Terramechanics*, 72, pp. 39-54.
24. Yakoub, R. Y., and Shabana, A. A., 2001, "Three-dimensional Absolute Nodal Coordinate Formulation for Beam Elements: Implementation and Applications", *ASME Journal of Mechanical Design*, 123(4), 614-621.
25. Mikkola, A. M., and Shabana, A. A., 2003, "A Non-Incremental Finite Element Procedure for the Analysis of Large Deformation of Plates and Shells in Mechanical System Applications", *Multibody Systems Dynamics*, 9, pp. 283-309.

26. Olshevskiy, A., Dmitrochenko, O., and Kim, C. W., 2014, "Three-dimensional Solid Brick Element using Slopes in the Absolute Nodal Coordinate Formulation", *ASME Journal of Computational and Nonlinear Dynamics*, 9(2), 021001.
27. Pappalardo, C. M., Wang, T., and Shabana, A. A., 2017, "On the Formulation of the Planar ANCF Triangular Finite Elements", *Nonlinear Dynamics*, 89(2), pp. 1019-1045.
28. Pappalardo, C. M., Wang, T., and Shabana, A. A., 2017B, "Development of ANCF Tetrahedral Finite Elements for the Nonlinear Dynamics of Flexible Structures", *Nonlinear Dynamics*, pp. 1-28, Accepted for publication, DOI: <https://doi.org/10.1007/s11071-017-3635-6>.
29. Bonet, J., and Wood, R.D., 1997, *Nonlinear Continuum Mechanics for Finite Element Analysis*, Cambridge University Press.
30. Ogden, R.W., 1984, *Non-Linear Elastic Deformations*, Dover Publications.
31. Shabana, A.A., and Mikkola, A., 2003, "Use of Finite Element Absolute Nodal Coordinate Formulation in Modeling Slope Discontinuity," *ASME Journal of Mechanical Design*, 125(2), pp. 342-350.
32. Shabana, A.A., and Maqueda, L.G., 2008, "Slope Discontinuities in the Finite Element Absolute Nodal Coordinate Formulation: Gradient Deficient Elements," *Multibody System Dynamics*, 20(3), pp. 239-249.
33. Aboubakr, A.K., and Shabana, A.A., 2015, "Efficient and Robust Implementation of the TLISMNI Method," *Journal of Sound and Vibration*, 353, pp. 220-242.
34. Li, B, Yang, X., Yang, J., Zhang, Y., and Ma, Z., 2016, "Optimization Algorithm Comparison for In-Plane Flexible Ring Tire Model Parameter Identification," *Proc. Of*

AMSE International Design Engineering Technical Conferences and Computers and Information in Engineering Conference, Charlotte, USA, August 21-24.

35. Shabana, A.A., 2010, *Computational Dynamics*, 3rd Edition, John Wiley and Sons, New York.

Table 1. Vehicle inertia properties

Components	Mass (kg)	I_{xx} (kg.m ²)	I_{yy} (kg.m ²)	I_{zz} (kg.m ²)
Chassis	708.35	156.83	1647.4	1767.3
Car body	1378.18	712.38	1952.25	2358.16
Front sub-frame	50.000	1.0000×10^{-6}	1.0000×10^{-6}	1.0000×10^{-6}
Rear sub-frame	45.359	2.9264×10^{-4}	2.9264×10^{-4}	2.9264×10^{-4}
Front left and right suspensions				
Upright	3.6382	4.0800×10^{-2}	4.2300×10^{-2}	8.3400×10^{-3}
Upper arm	5.4431	2.3300×10^{-2}	3.6100×10^{-2}	1.3200×10^{-2}
Lower arm	16.329	0.14688	0.23163	0.11852
Upper strut	5.0000	1.0000×10^{-6}	1.0000×10^{-6}	1.0000×10^{-6}
Lower strut	5.0000	1.0000×10^{-6}	1.0000×10^{-6}	1.0000×10^{-6}
Tire	68.039	1.1998	1.7558	1.1998
Tierod	0.5545	5.7854×10^{-3}	5.7854×10^{-3}	1.7745×10^{-5}
Tripot	1.9851	1.1019×10^{-3}	1.1019×10^{-3}	8.1390×10^{-4}
Drive shaft	4.2175	0.16599	0.16599	6.9283×10^{-4}
Spindle	1.1028	4.7790×10^{-4}	4.7790×10^{-4}	4.9628×10^{-4}
Rear left and right suspensions				
Upright	3.6382	4.0800×10^{-2}	4.2300×10^{-2}	8.3400×10^{-3}
Upper arm	5.9320	0.068400	0.091400	0.024000
Lower arm	16.287	0.29036	0.51811	0.23229
Upper strut	0.45359	2.9264×10^{-4}	2.9264×10^{-4}	2.9264×10^{-4}
Lower strut	0.45359	2.9264×10^{-4}	2.9264×10^{-4}	2.9264×10^{-4}
Tire	68.039	1.1998	1.7558	1.1998
Tierod	2.0412	4.2200×10^{-2}	4.2200×10^{-2}	1.9000×10^{-4}
Tripot	2.0307	1.1383×10^{-3}	1.1383×10^{-3}	8.4254×10^{-4}
Drive shaft	6.0495	0.24565	0.24565	1.4463×10^{-3}
Spindle	1.5046	7.7539×10^{-4}	7.7539×10^{-4}	9.2387×10^{-4}

Table 2. Ideal joints used in vehicle model

Joint type	Number of joints
Spherical/ball	25
Revolute/pin	16
Rigid/bracket	4
Cylindrical	8
Relative angular velocity	5
Gear	8
Rack pinion	1

Table 3. Compliant joint elements used in vehicle model

Joint type	Number of elements
Bushing	4
Bearing	16

Table 4. Chassis frequencies

Mode number	Frequency (Hz)
1	30.9
2	65.35
3	70.48
4	74.27
5	78.23
6	82.08
7	91.98
8	95.38
9	97.21
10	99.28
11	116.21
12	121.45
13	129.75
14	137.83
15	148.87

Table 5. Brush tire parameters

Parameter	Value
Radial stiffness (MN/m)	2
Radial damping (MN.s/m)	1
Longitudinal slip stiffness (MN/m ²)	10
Lateral slip stiffness (kN/deg.m ²)	50
Friction coefficient	0.8
Rolling resistance coefficient	0.03

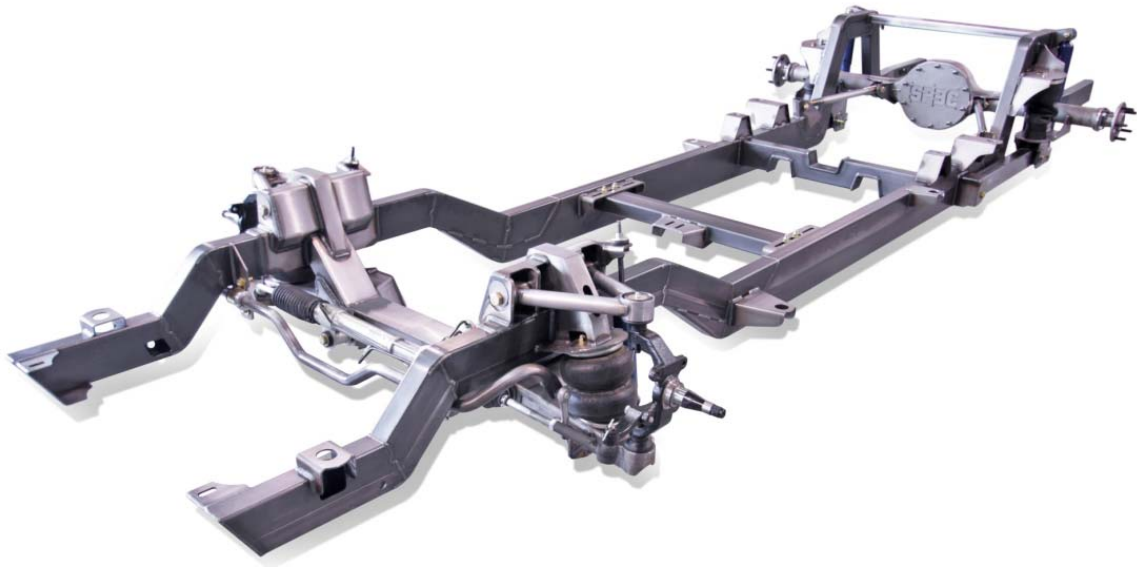


Figure 1. Structural discontinuities in a truck chassis (<http://roadstershop.com/product/full-chassis/1967-72-c10-truck-spec-chassis/>)



Figure 2. Pneumatic off-road tire (upper figure) and airless off-road tire (lower figure)

(Upper figure: <http://www.nittotire.com/light-truck-tires/trail-grappler-mud-terrain-light-truck-tire/>; lower figure: <http://croctyres.com.au/wp-content/uploads/2015/12/image10.jpg/>)

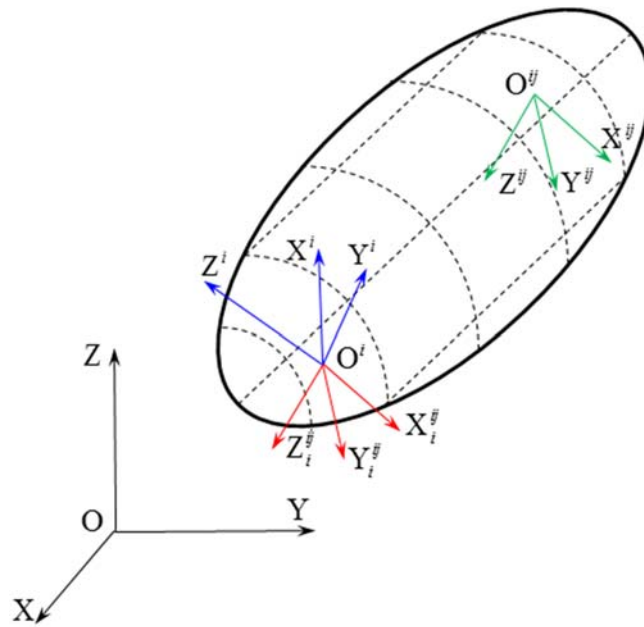


Figure 3. Coordinate systems involved in FE-FFR formulation (Black: GCS; Blue: BCS; Red: ICS; Green: ECS)

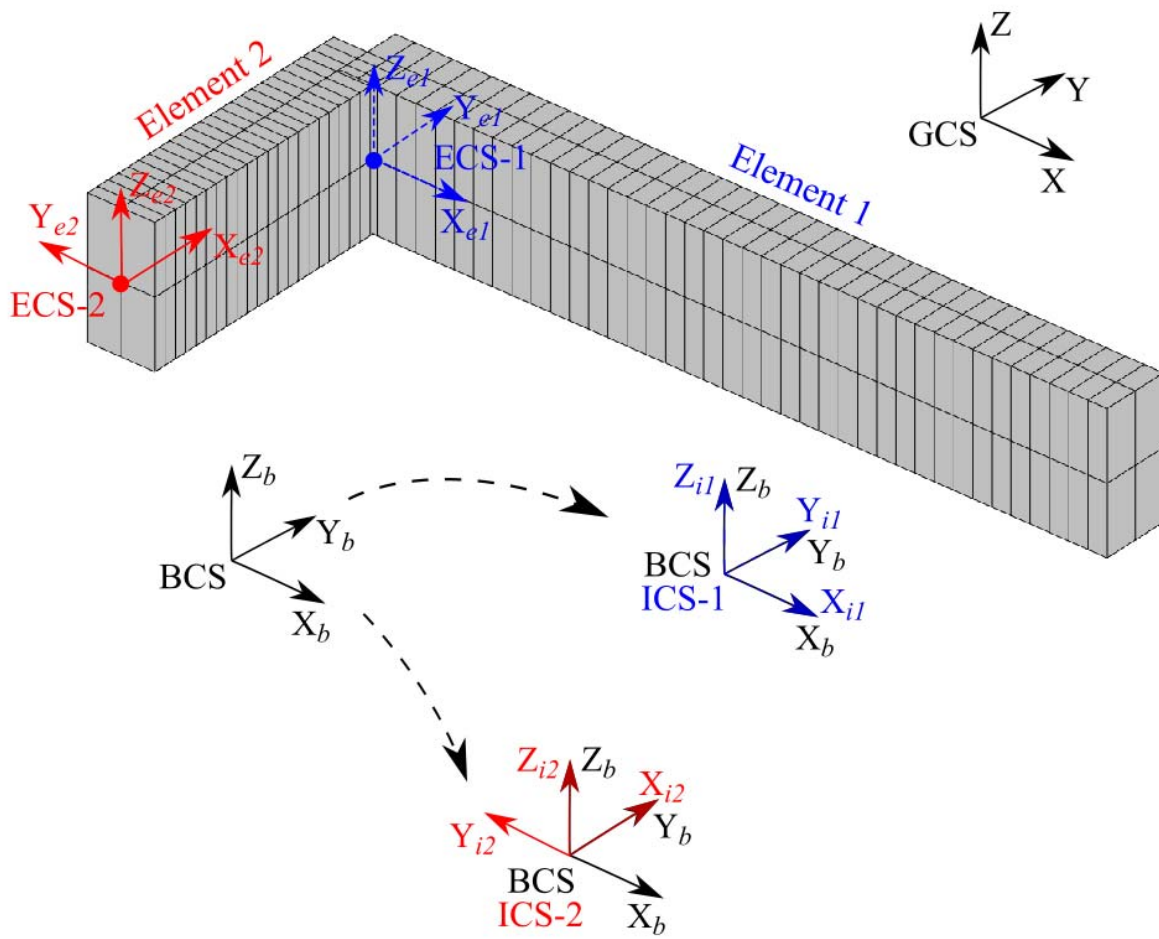


Figure 4. FE-FFR structural discontinuity (subscripts b , i and e correspond to BCS, ICS and ECS respectively)

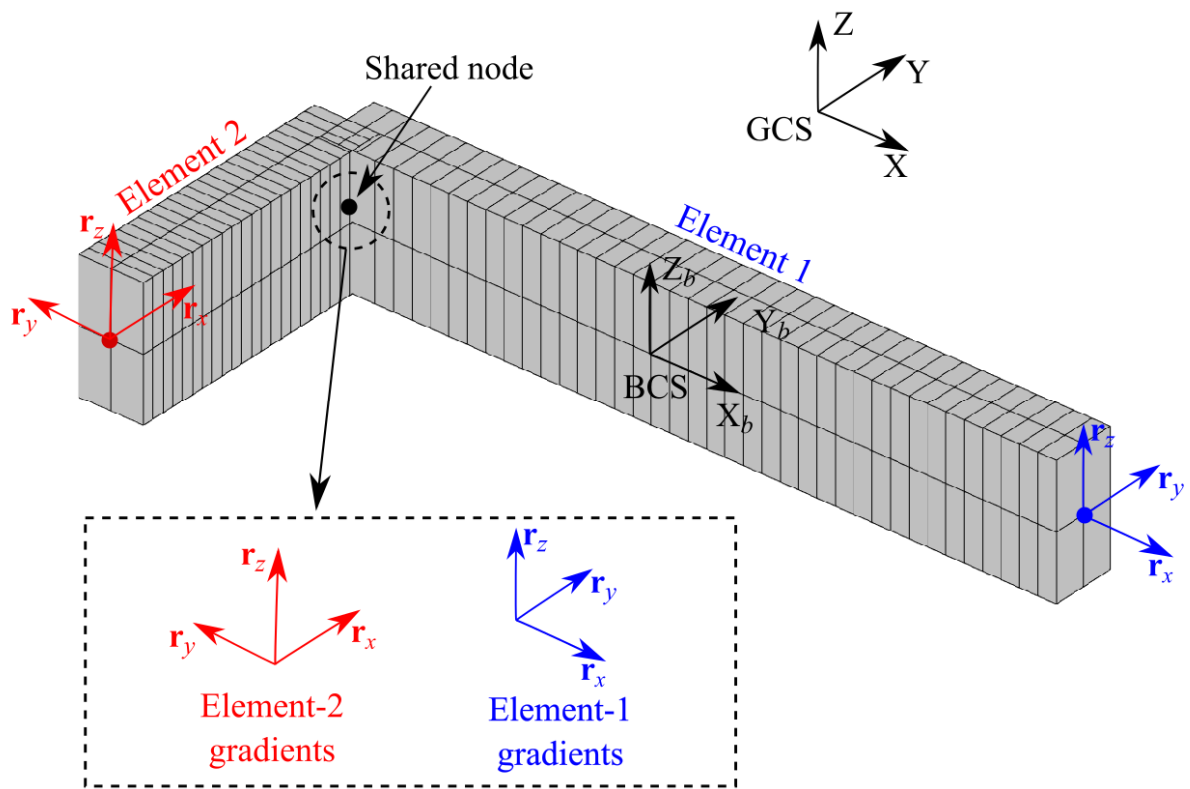


Figure 5. ANCF structural discontinuity

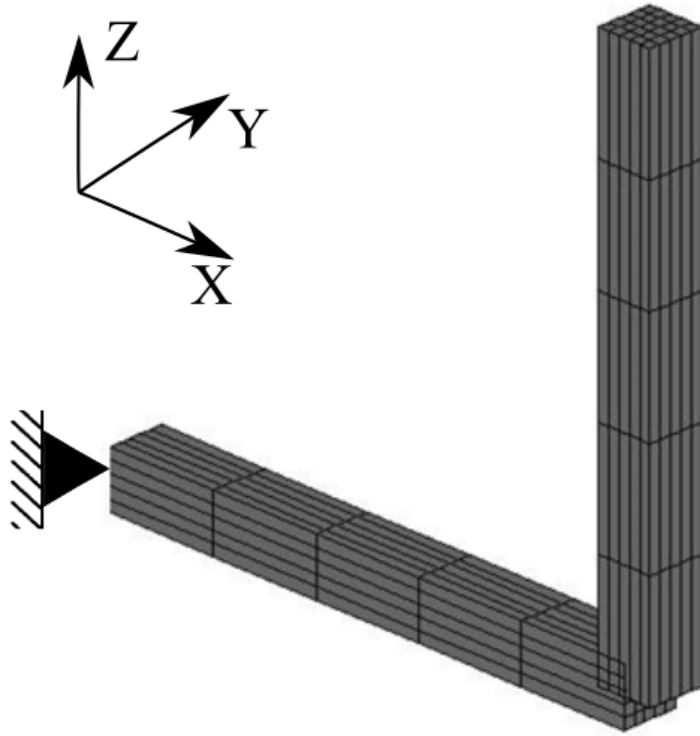


Figure 6. L-shaped beam pendulum with structural discontinuity

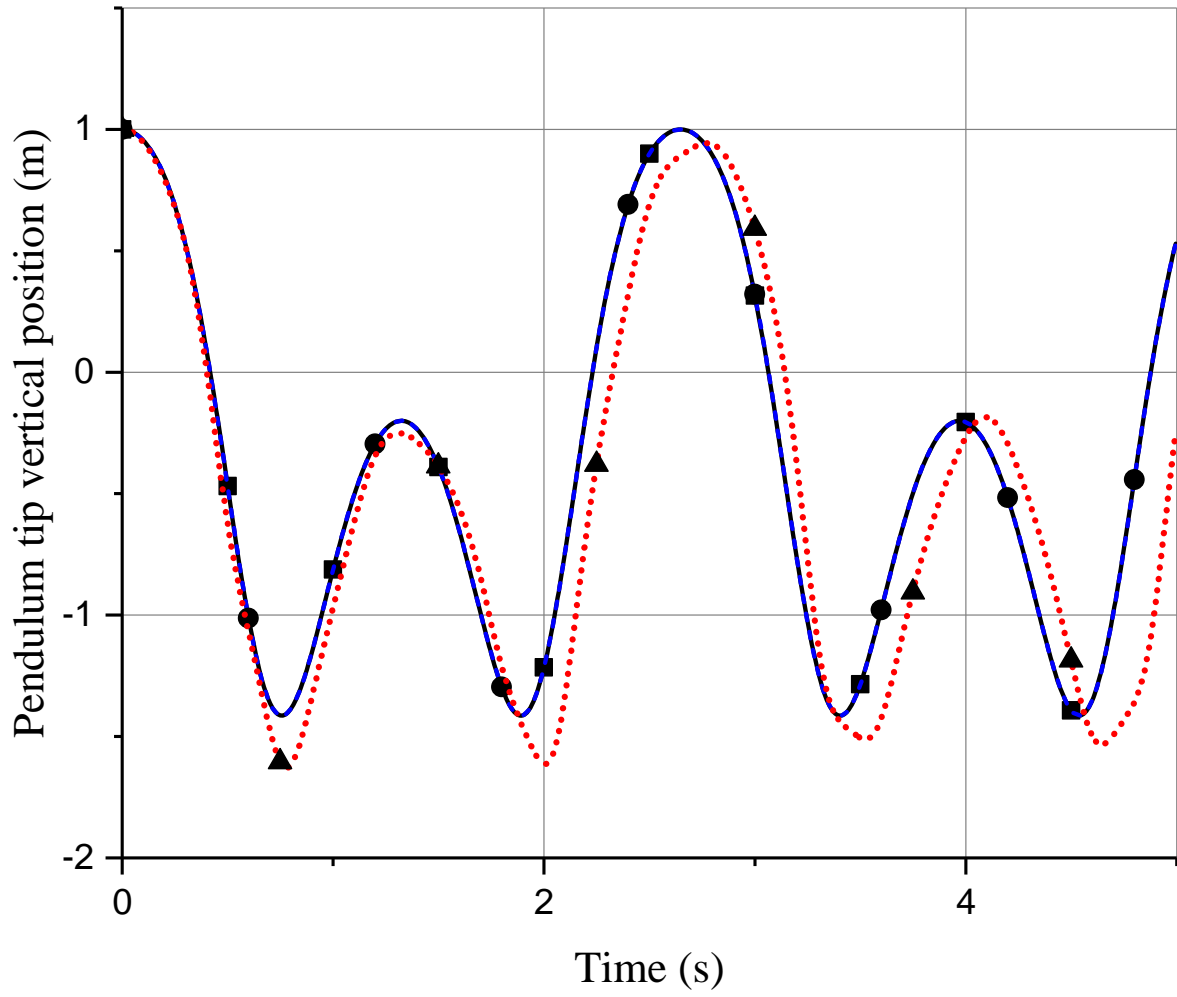


Figure 7. L-shaped beam tip vertical position: ANCF and rigid body model comparison (

—■— Rigid; - -●- ANCF ($E = 2 \times 10^{12}$ Pa); ···▲··· ANCF ($E = 2 \times 10^7$ Pa))

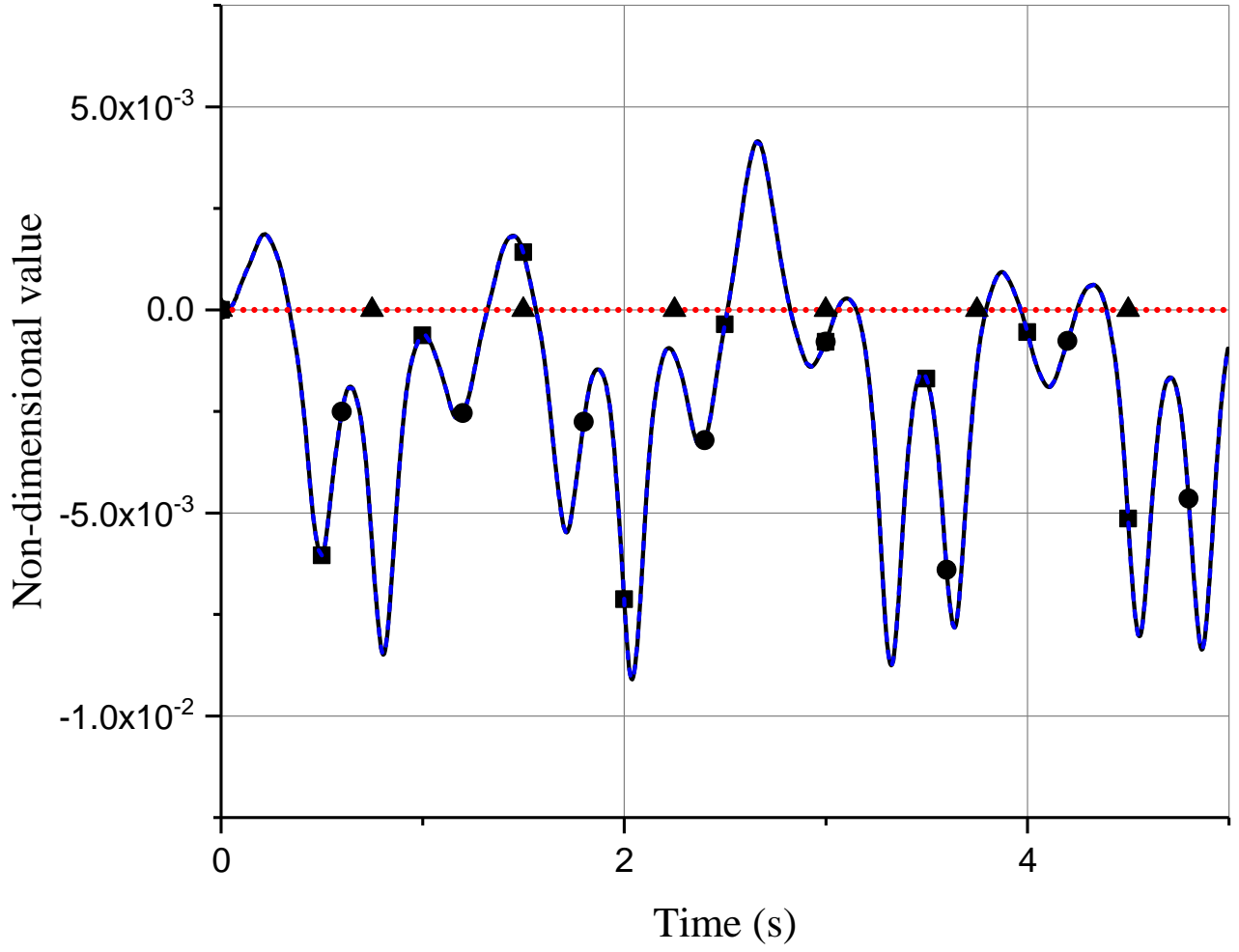


Figure 8. ANCF L-shaped beam engineering shear strain and cosine of angle at structural discontinuity

$$(\text{---} \blacksquare \text{---} \mathbf{r}_{x_1}^T \mathbf{r}_{x_2} ; \text{---} \bullet \text{---} \mathbf{r}_{x_1}^T \mathbf{r}_{z_1} ; \text{---} \blacktriangle \text{---} \mathbf{r}_{x_1}^T \mathbf{r}_{x_2} - \mathbf{r}_{x_1}^T \mathbf{r}_{z_1})$$

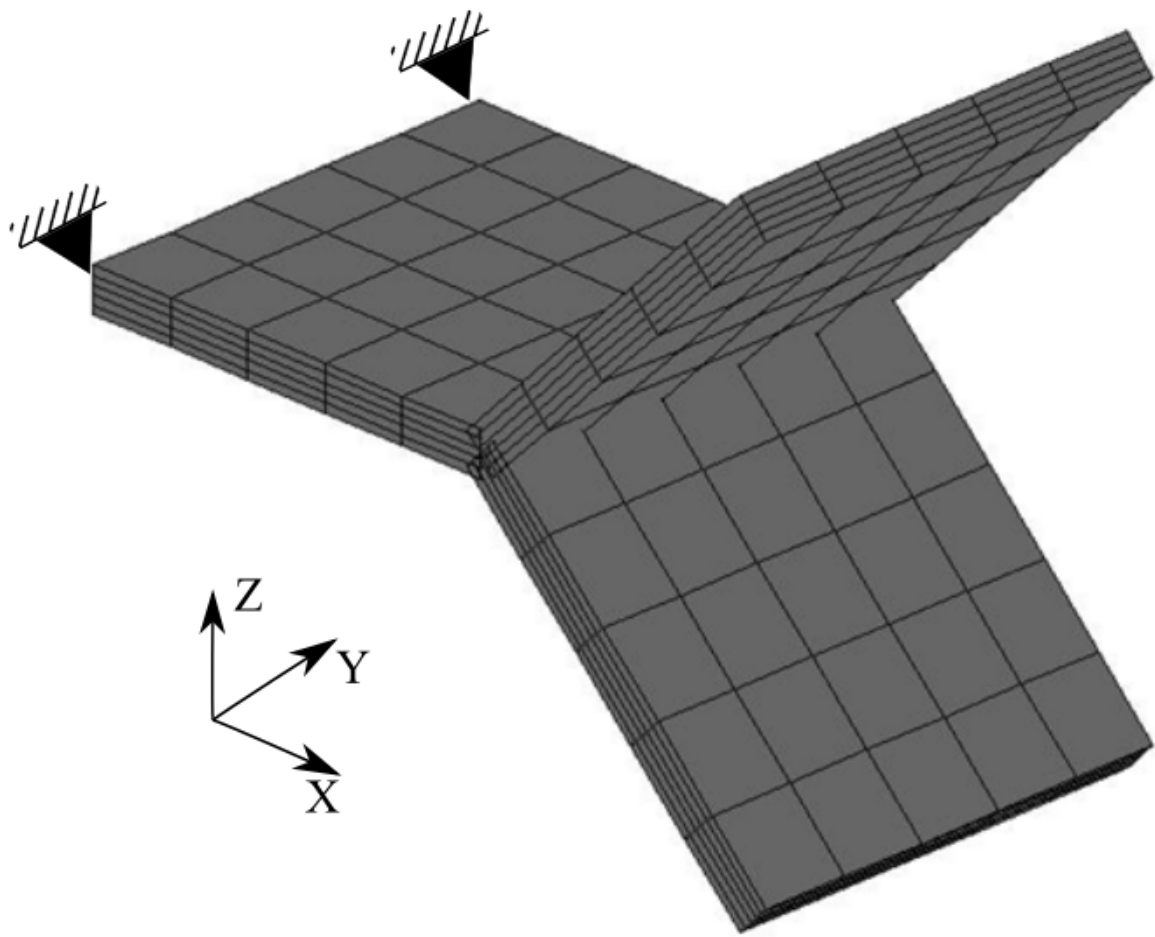


Figure 9. Y-shaped plate/shell pendulum model

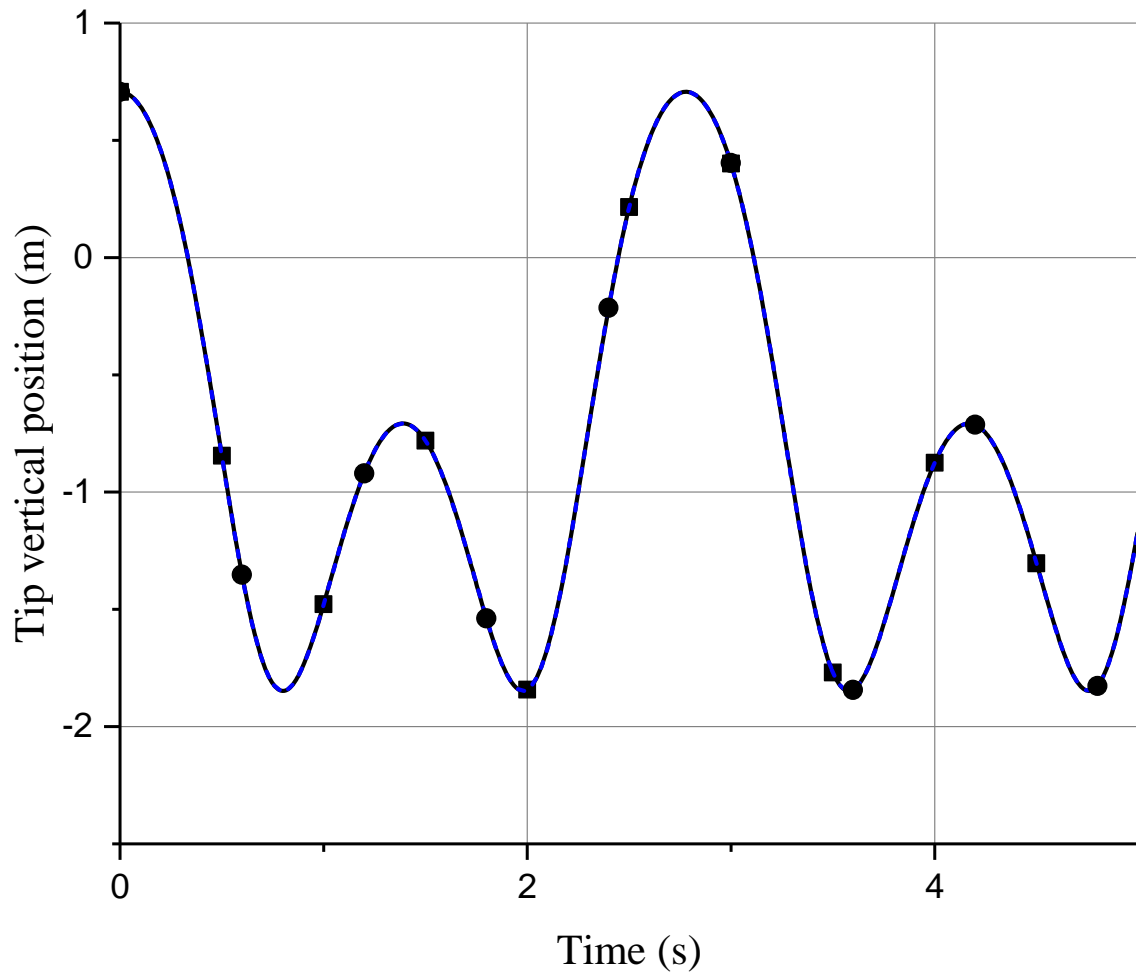


Figure 10. Y-shaped plate/shell pendulum tip vertical position: ANCF and rigid body model

comparison (—■— Rigid; - -●- - ANCF $E = 2 \times 10^{12}$ Pa)

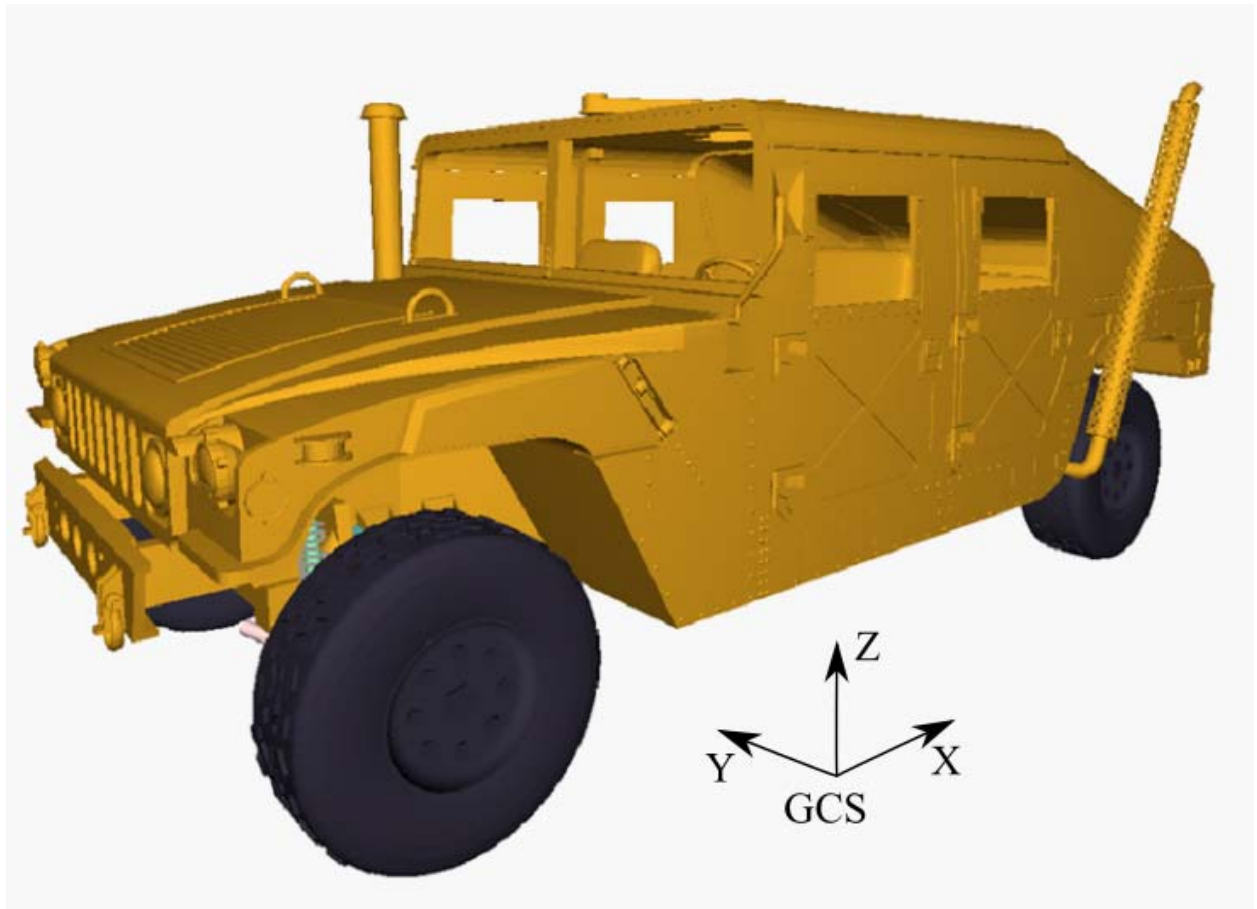


Figure 11. Off-road wheeled vehicle model (GCS: global coordinate system for orientation reference)

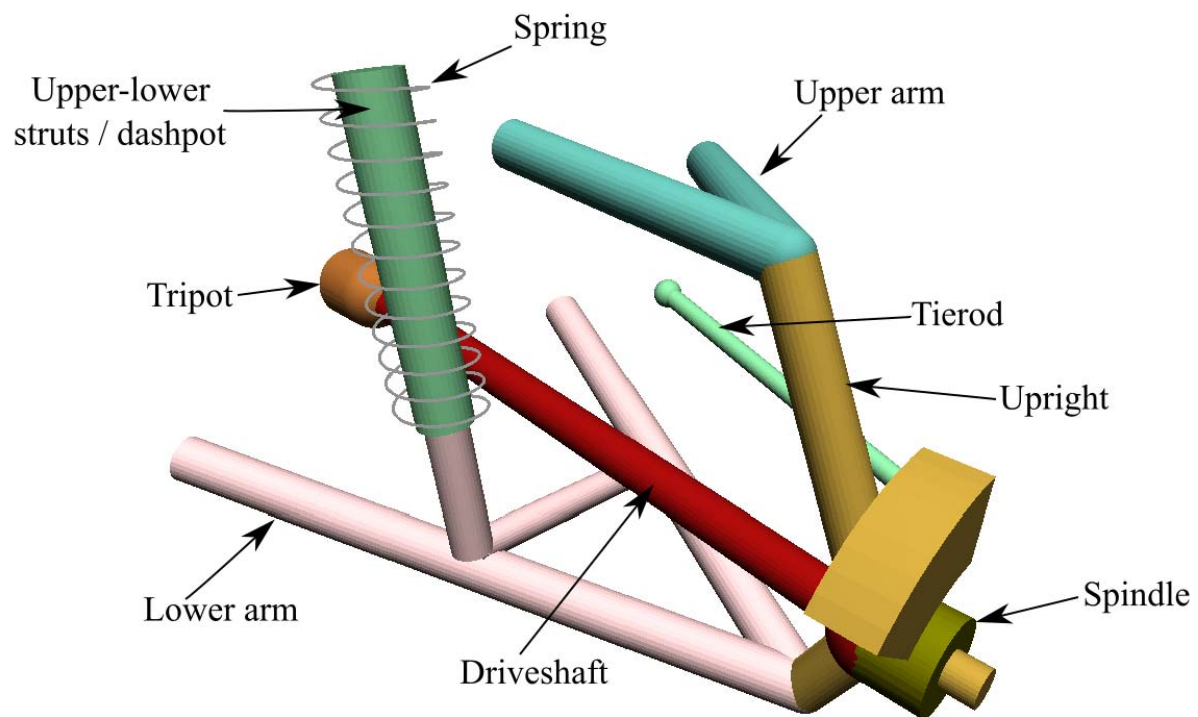


Figure 12. Front left suspension close-up

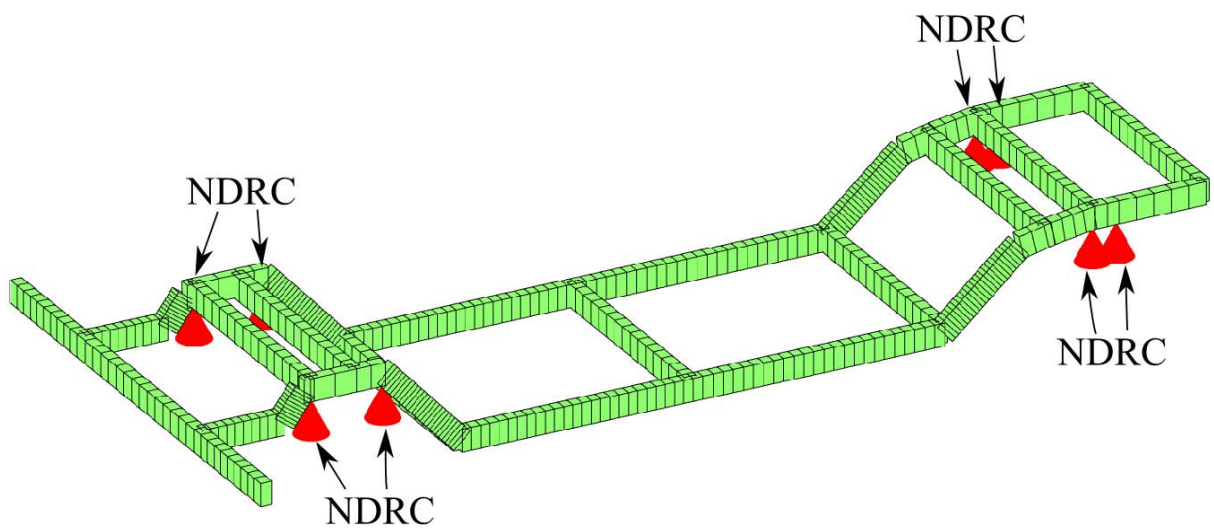


Figure 13. FFR chassis mesh (NDRC: nodal displacement reference conditions)

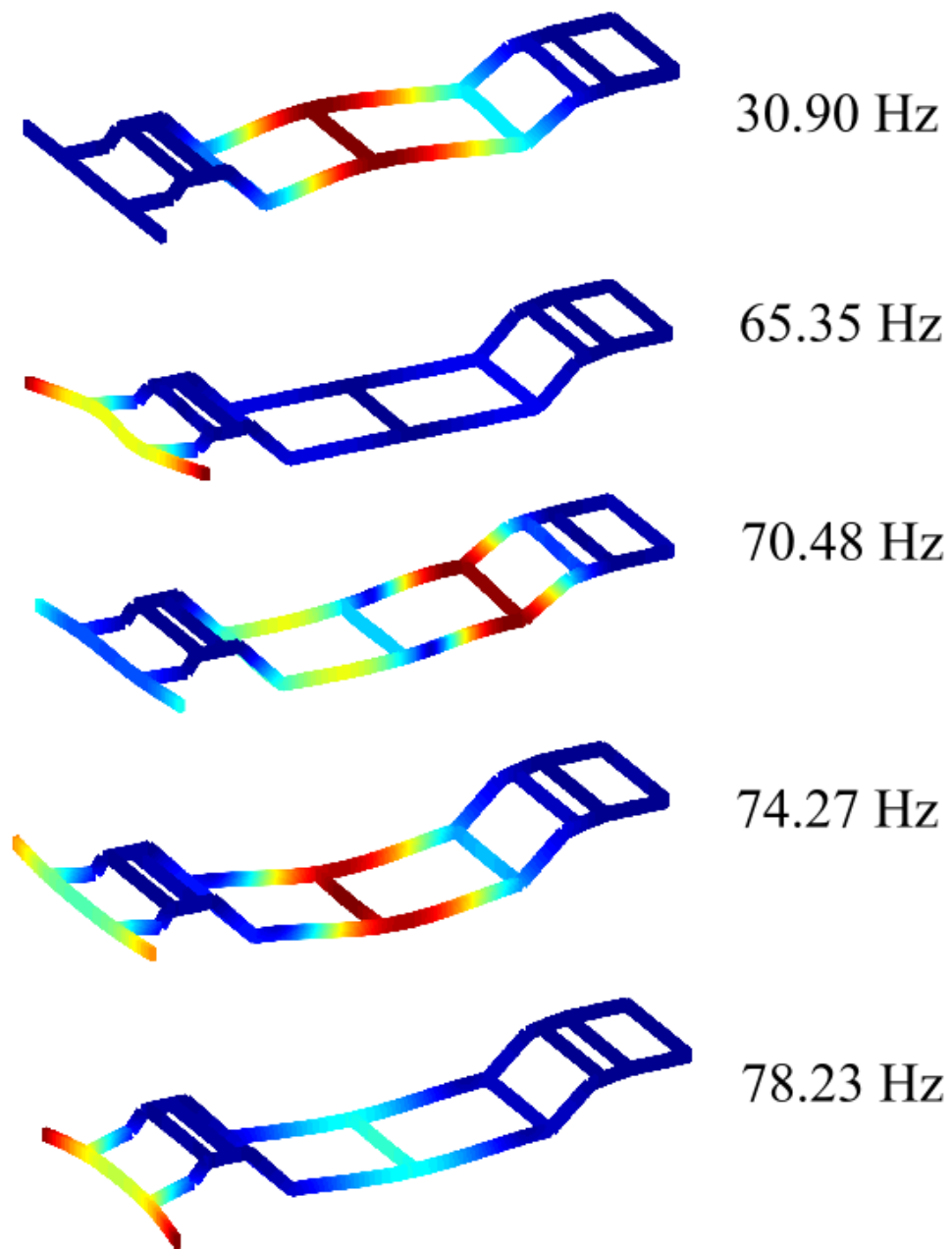


Figure 14. FFR chassis first five mode shapes and frequencies

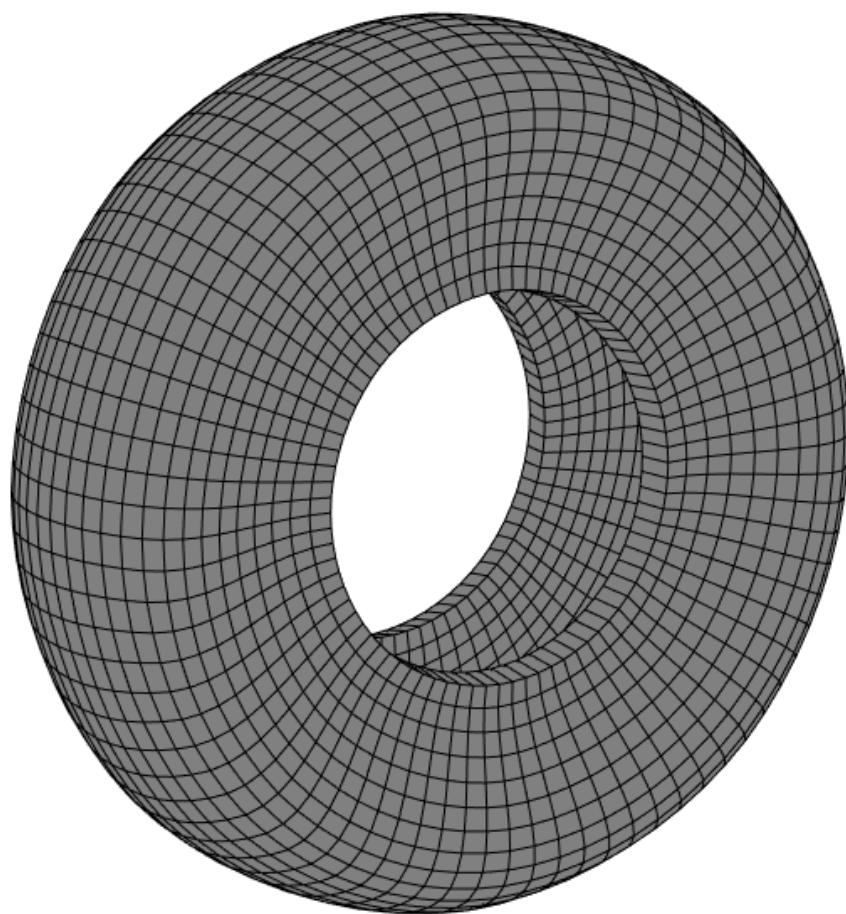


Figure 15. ANCF pneumatic tire

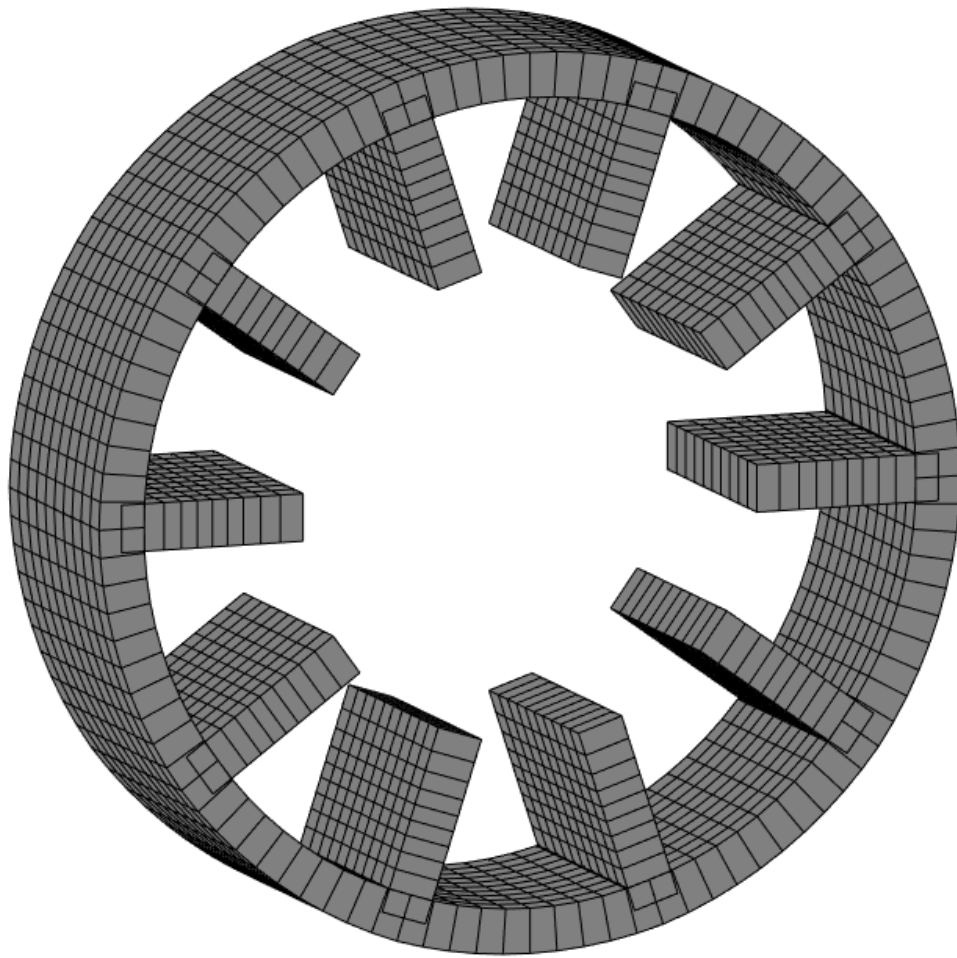


Figure 16. ANCF airless tire

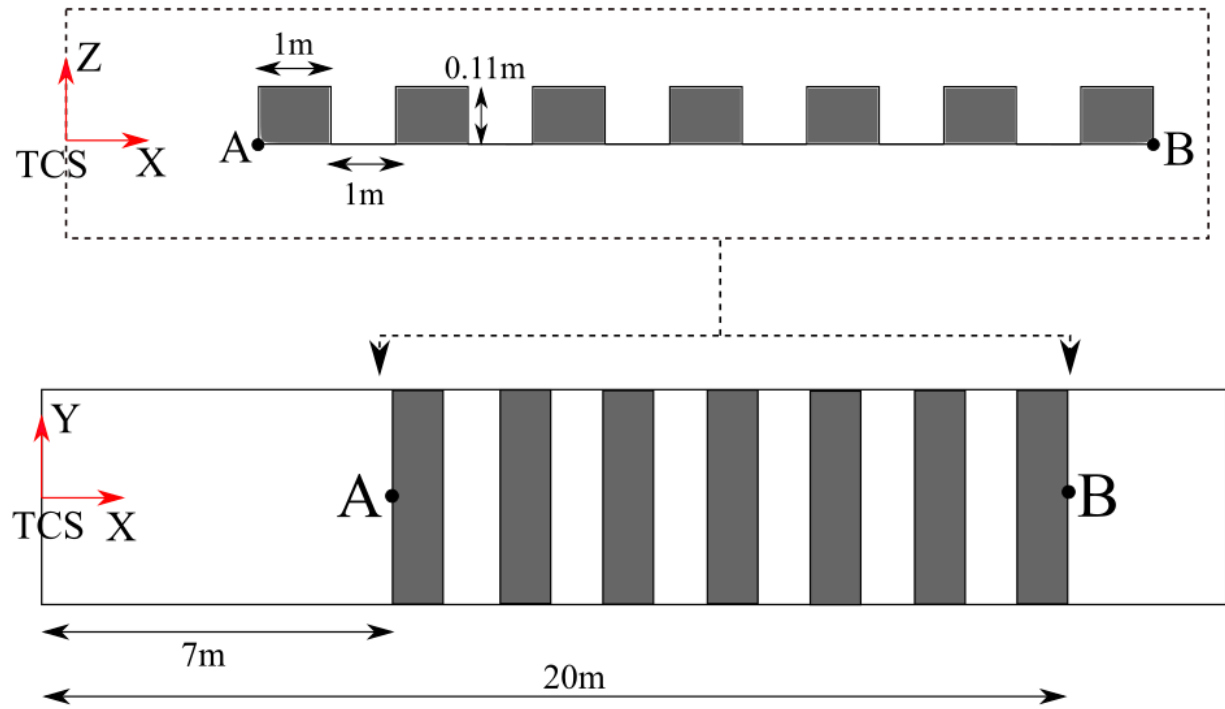


Figure 18. Durability vehicle simulation test track (TCS: track coordinate system, whose location coincides with the global coordinate system)

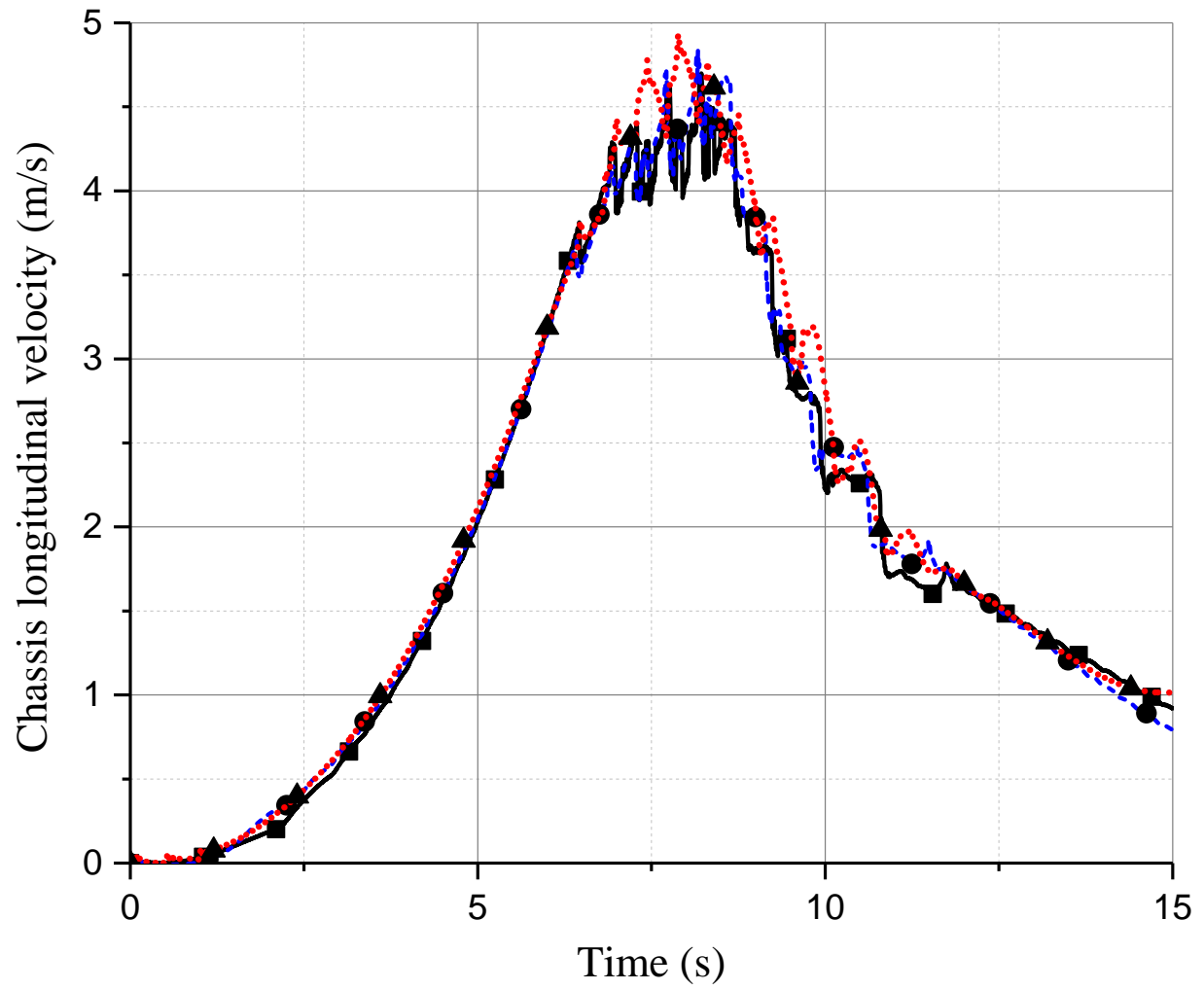


Figure 19. Chassis longitudinal velocity (—■— Airless; - -●- - Pneumatic; ···▲··· Brush)

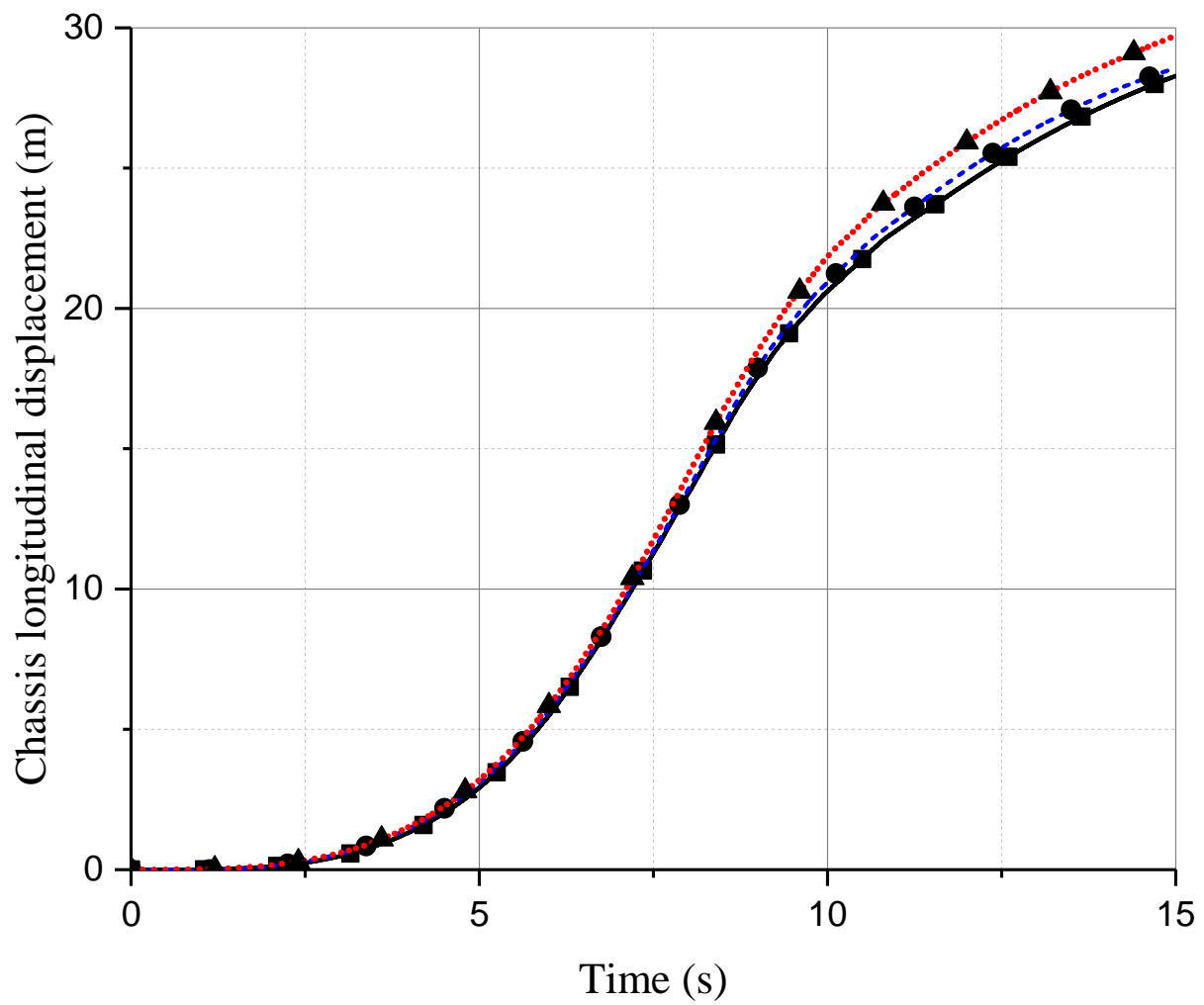


Figure 20. Chassis longitudinal displacement (—■— Airless; - - -●- - Pneumatic; ····▲···· Brush)

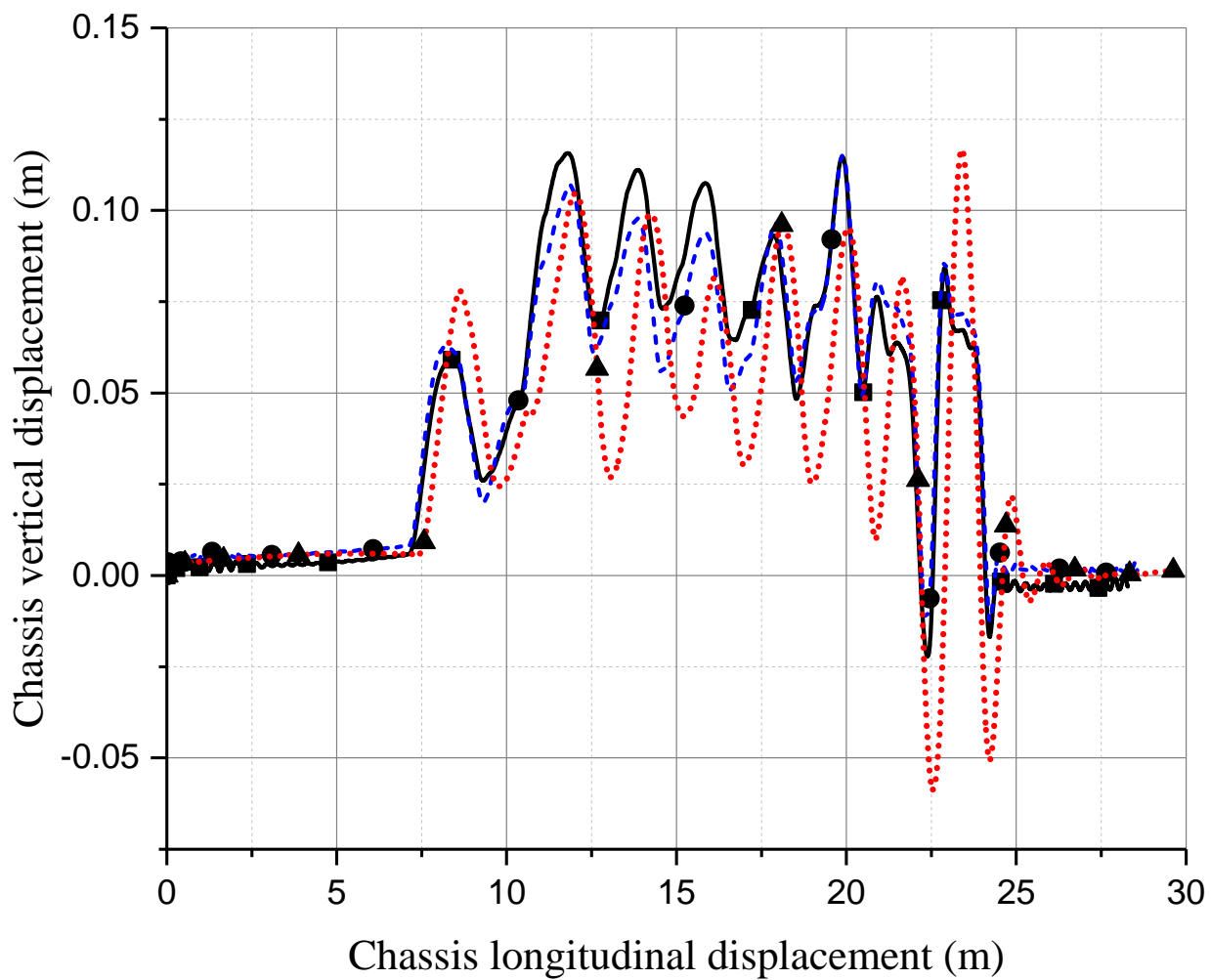


Figure 21. Chassis vertical displacement (—■— Airless; - -●- - Pneumatic; ...▲... Brush)

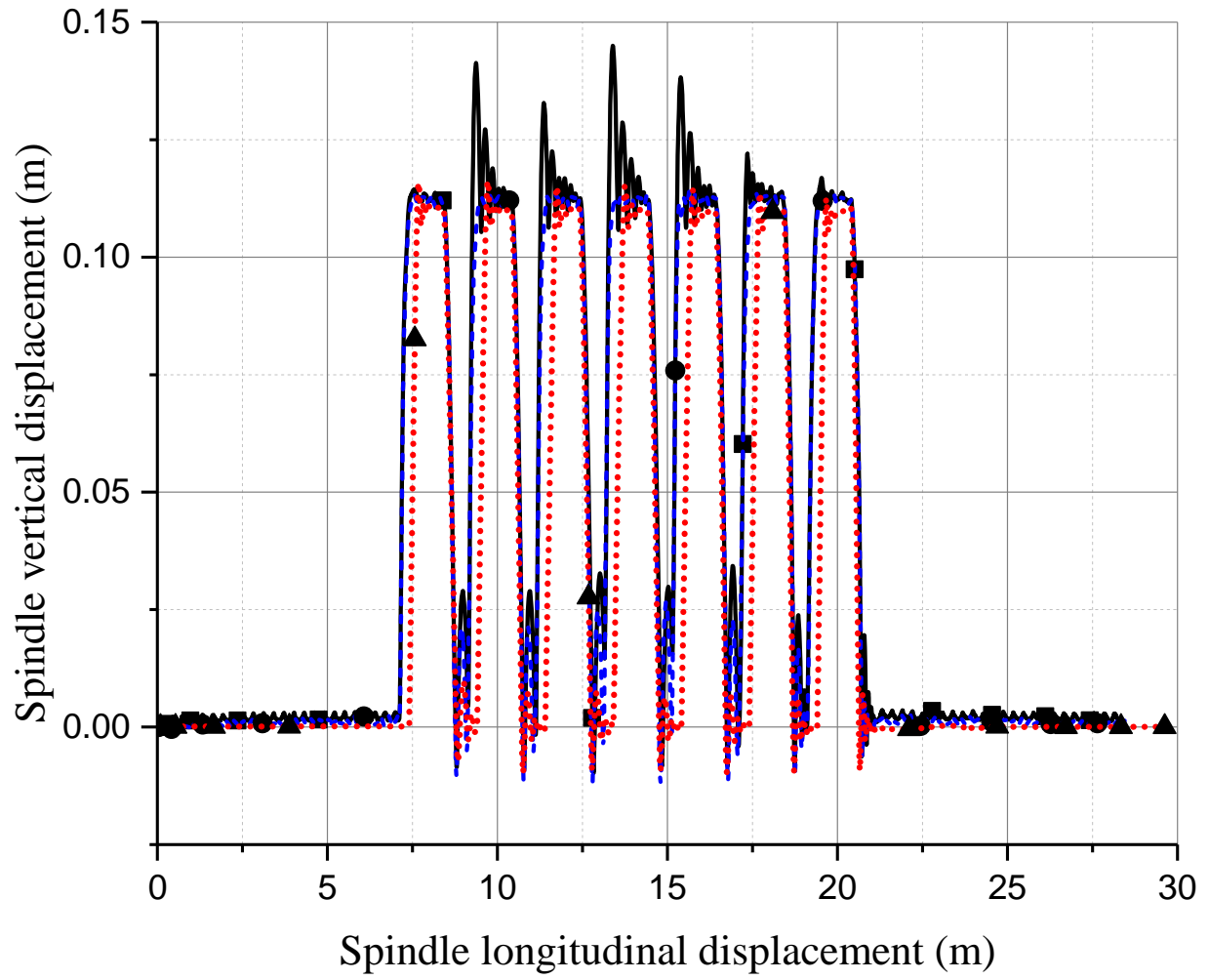


Figure 22. Front left spindle vertical displacement (—■— Airless; - - ● - - Pneumatic; . . . ▲ . . . Brush)

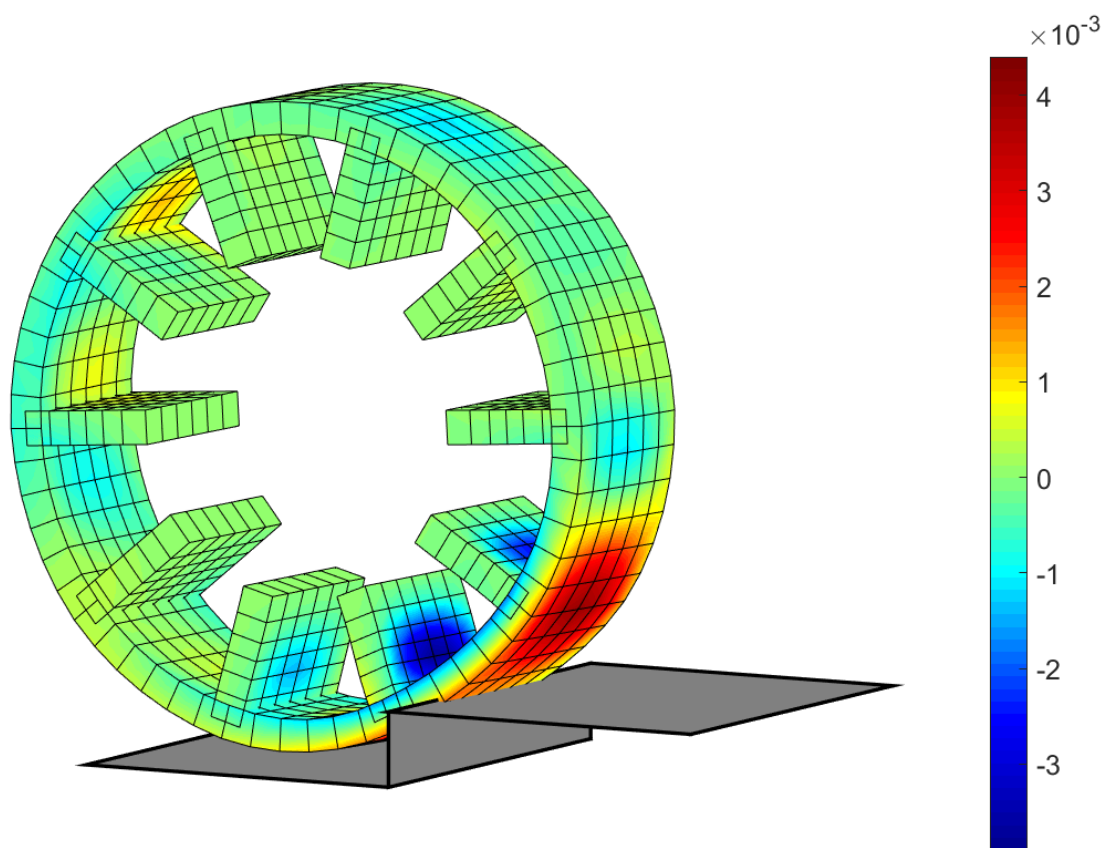


Figure 23. Airless tire hitting second bump with ε_{yy} strain contours

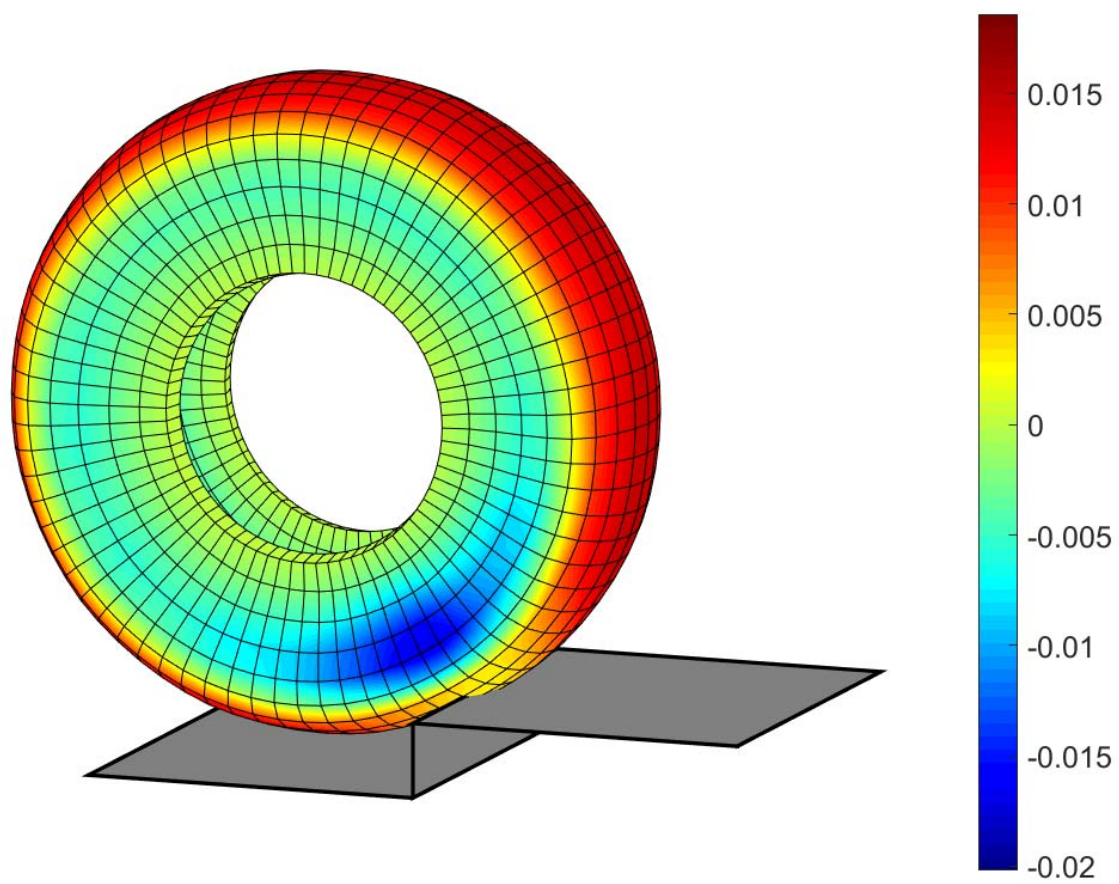


Figure 24. Pneumatic tire hitting second bump with ε_{yy} strain contours

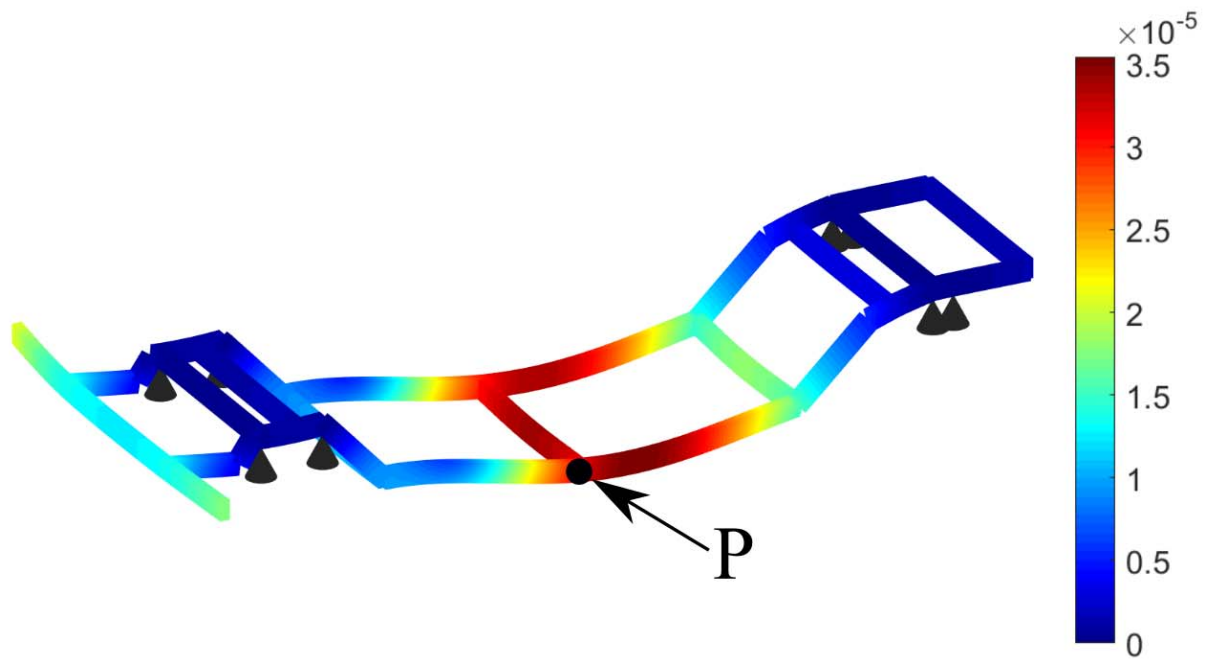


Figure 25. FFR chassis total deformation instance during dynamic simulation (with deformation contours)

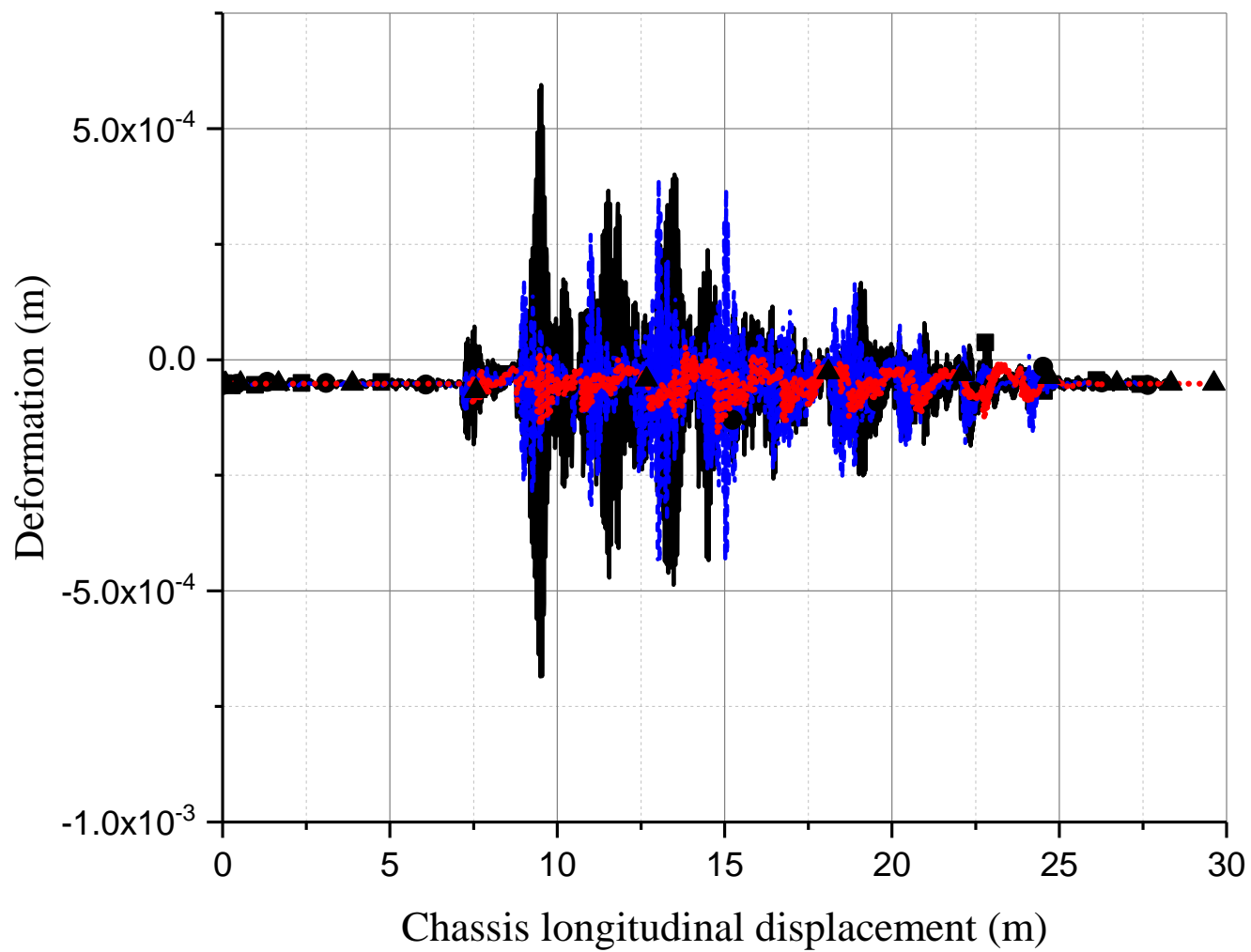


Figure 26. Vertical deformation at chassis point P with respect to BCS (—■— Airless;

---●--- Pneumatic; ...▲... Brush)

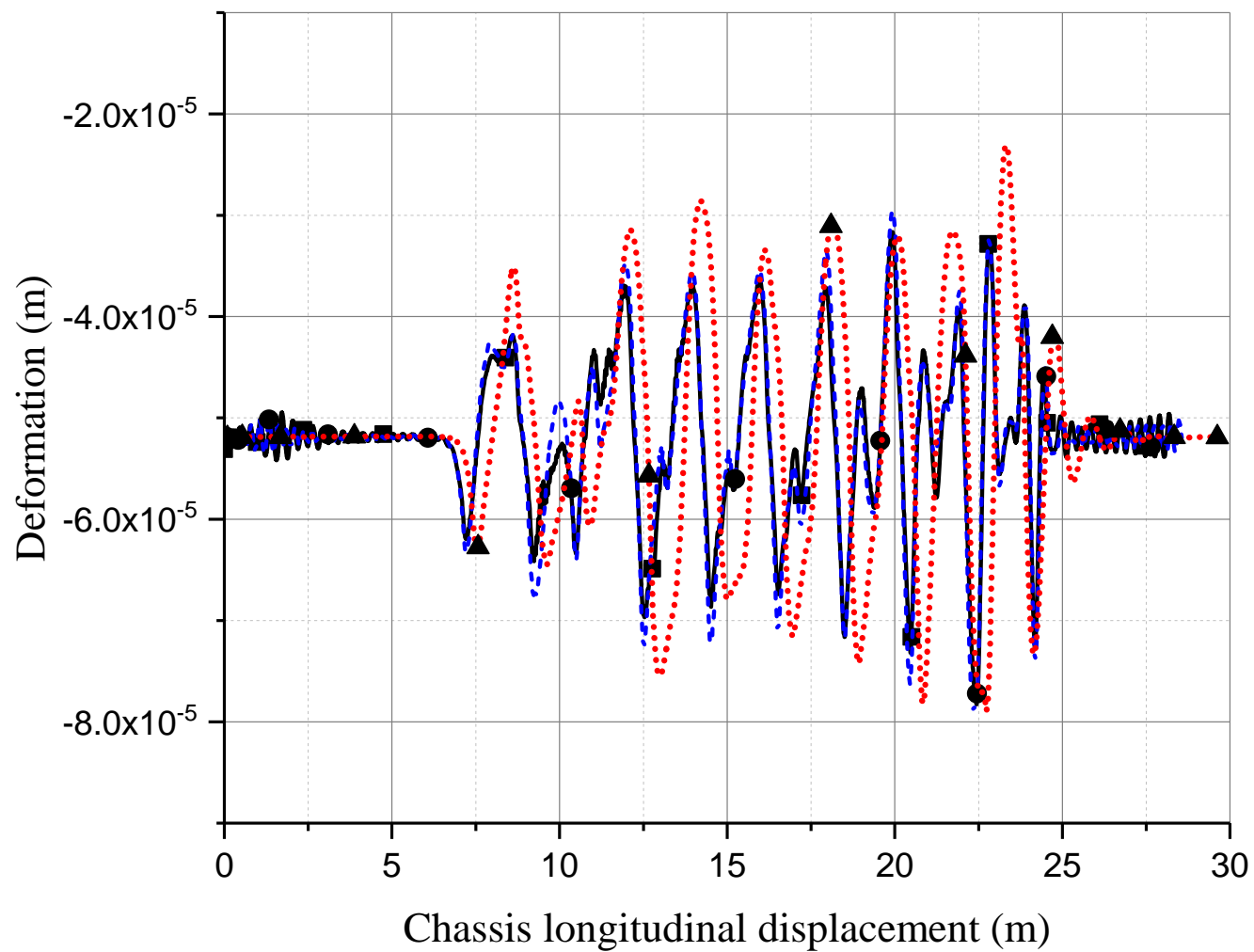


Figure 27. Vertical deformation at chassis point P with respect to BCS after applying low-pass

filter (—■— Airless; - -●- - Pneumatic; ···▲··· Brush)

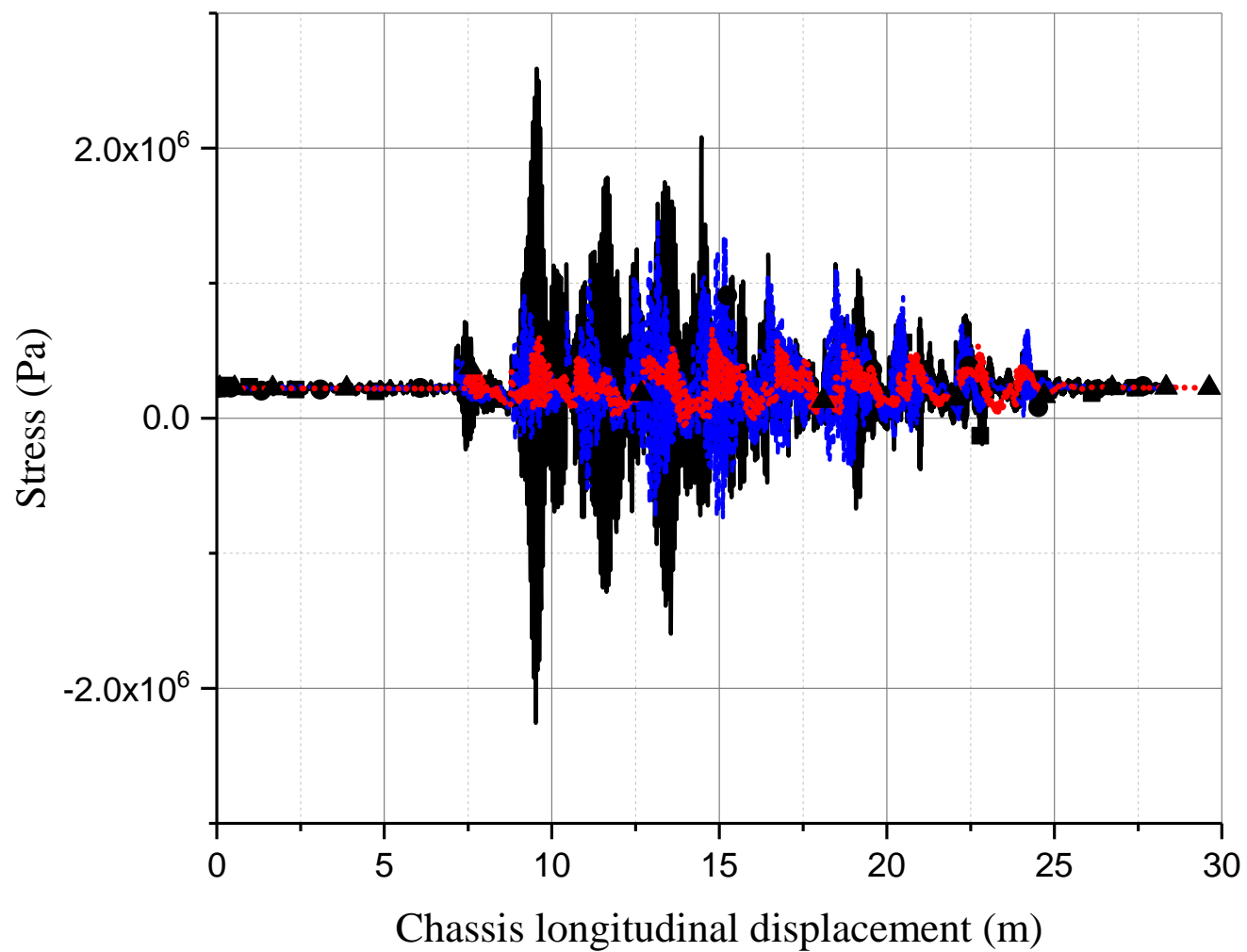


Figure 28. Axial stress at chassis point P with respect to BCS (—■— Airless; - -●- - Pneumatic;▲..... Brush)

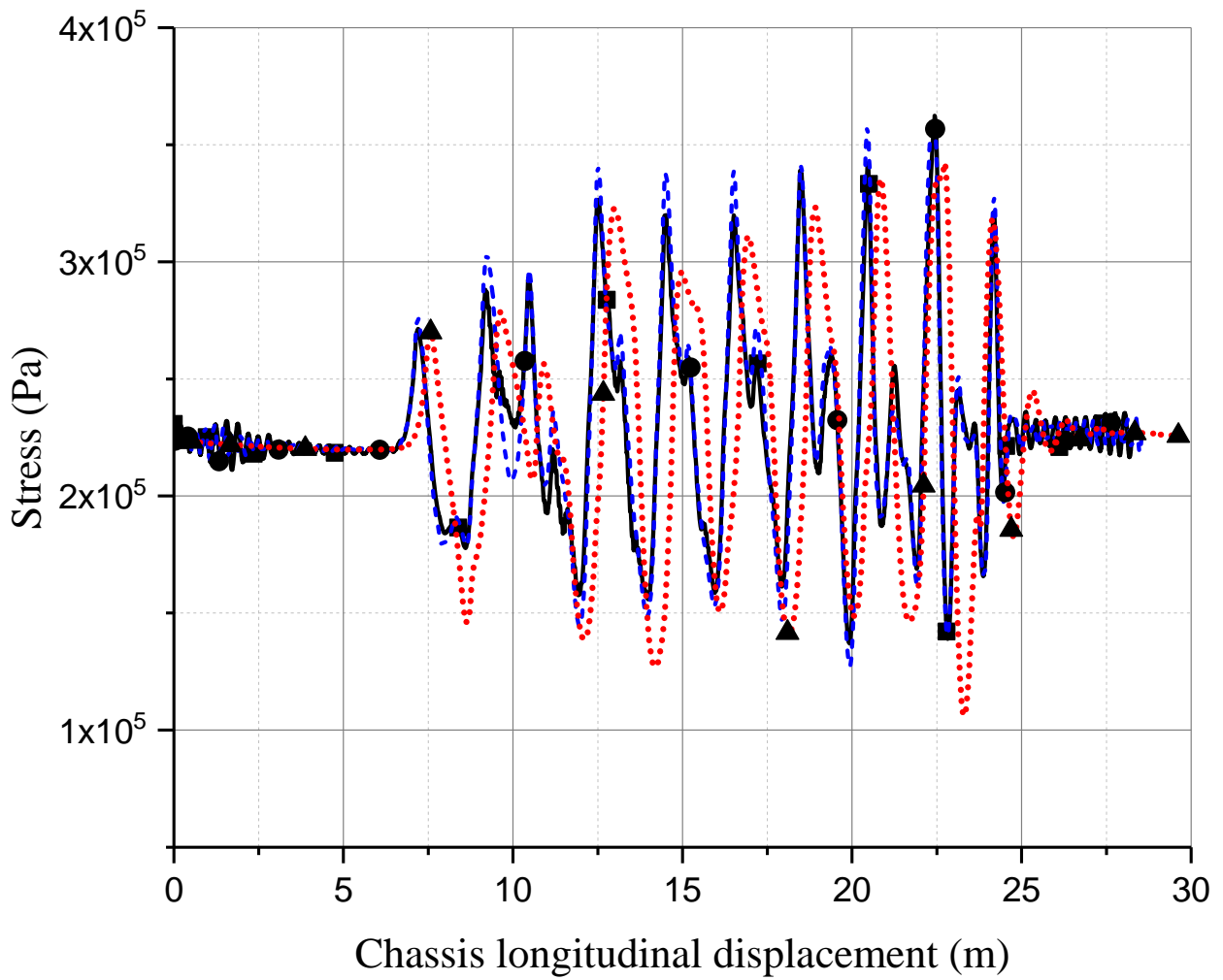


Figure 29. Axial stress at chassis point P with respect to BCS after applying low-pass filter (

—■— Airless; - -●- - Pneumatic; ····▲···· Brush)

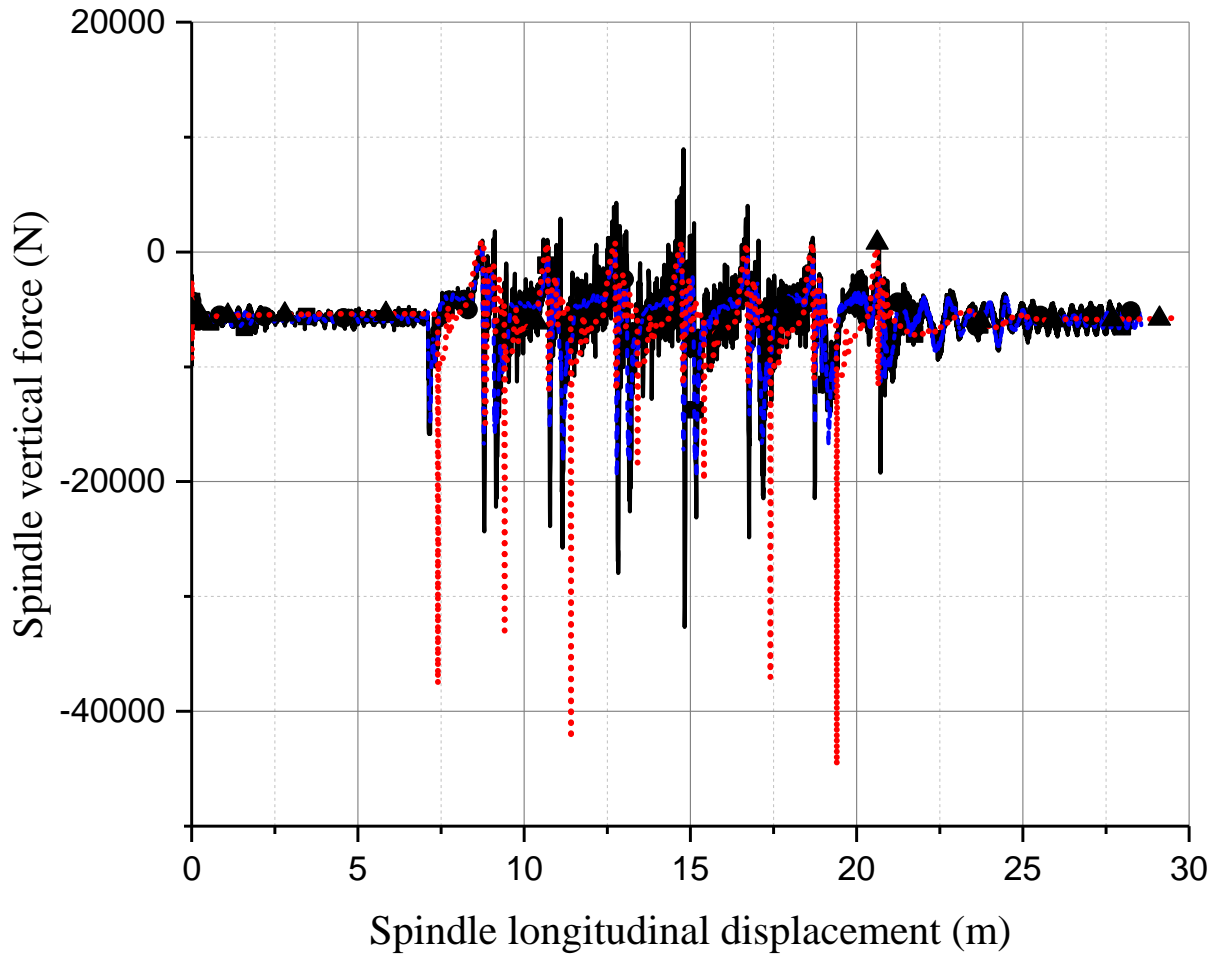


Figure 30. Front left spindle vertical force (—■— Airless; - -●- - Pneumatic; ···▲··· Brush)

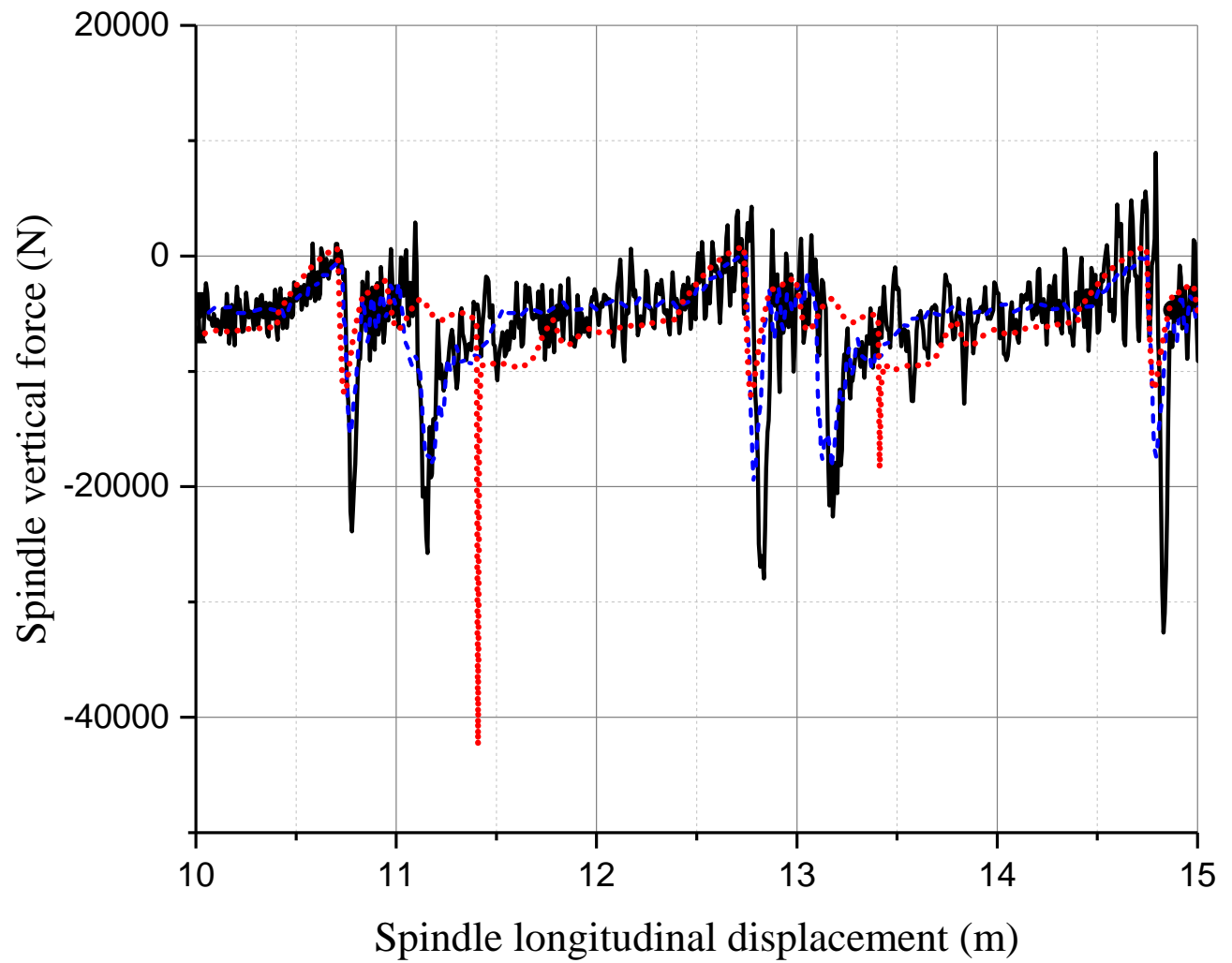


Figure 31. Front left spindle vertical force: zoomed in for 10-15m segment (—■— Airless; ---●--- Pneumatic;▲..... Brush)

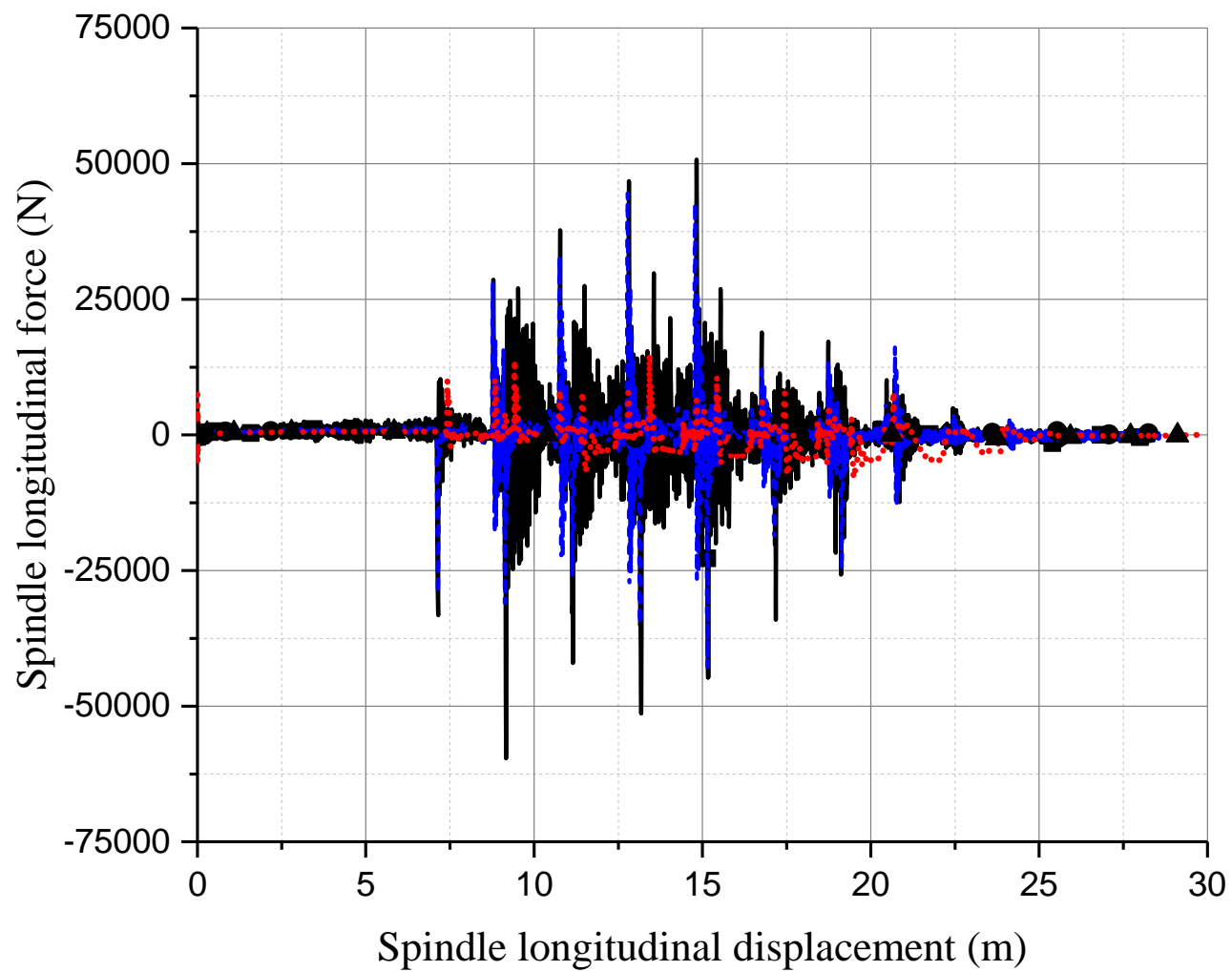


Figure 32. Front left spindle longitudinal force (—■— Airless; - -●- - Pneumatic;▲..... Brush)

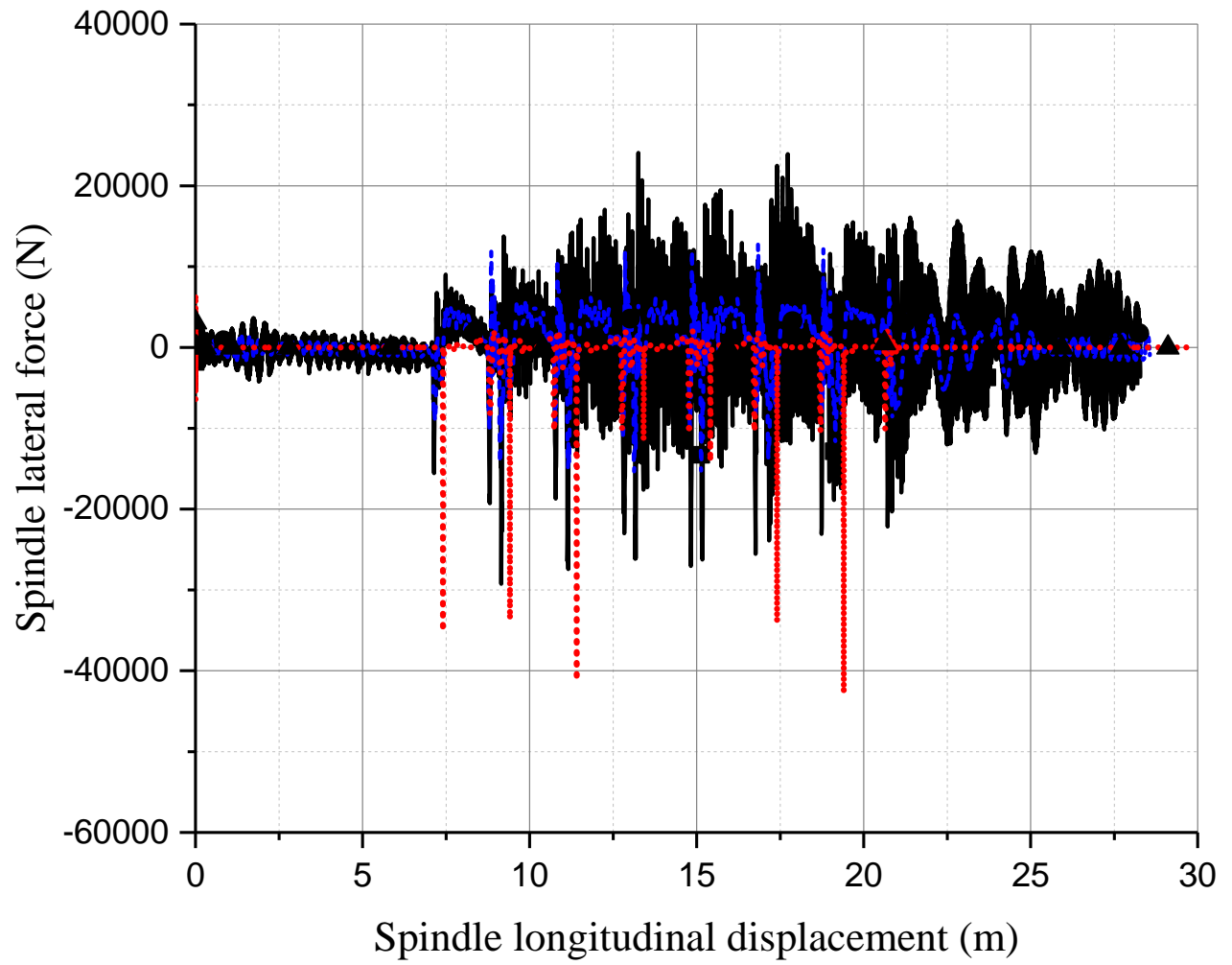


Figure 33. Front left spindle lateral force (—■— Airless; - -●- - Pneumatic; ···▲··· Brush)